Toward a homogenizing machine

Thibault Dassonville, Martin Poncelet, Nicolas Auffray

Toward a homogenizing machine

Thibault Dassonville[b,a,*], Martin Poncelet[a], Nicolas Auffray[b]

[a] *LMT (ENS Paris-Saclay/CNRS/Université Paris Saclay), 61 avenue du Président Wilson, F-94235 Cachan, France*
[b] *Université Paris-Est, Laboratoire de Modélisation et Simulation Multi Echelle, UMR 8208 CNRS, 5 Boulevard Descartes, 77454 Marne-la-Vallée Cedex 2, France*

Abstract

The idea of an experimental homogenization device adapted to the case of architectural materials is discussed here. Although more advanced homogenization schemes exist, the case of average-field homogenization by KUBC within the framework of linear elasticity is studied here because of its (relative!) simplicity of adaptation to an experimental setup. The main idea here is to propose a device that is simple to implement, inexpensive but that allows to apply a load as close as possible to a perfect KUBC thanks to the use of pantographs to distribute the displacements on the edges of the specimen. For the purposes of the design and tests-design, a reduced model of the device has been developed.

Keywords:
Architectured materials, Experimental testing, Homogenisation, Boundary Conditions, Full-field measurement.

1. Introduction

1.1. Purpose

Expectations on materials in terms of multi-functional properties and mass saving are constantly increasing. For instance for industries as automotive or aerospace, gains in mass not only imply matter saving but also lead to significant enhancing the overall performance of the designed devices.

One of the possible answers to lighten structures is the use of architectured materials. For such materials, the matter is organised at different intermediary scales between the microstructure and the macroscopic shape. Their inner structure can be various, ranging from randomly distributed

*Corresponding author *Email: thibault.dassonville@u-pem.fr*

phases to a perfectly organized architectured. In the last case, we are in the realm of periodic materials and the mesoscopic scale is composed of a basic cell repeated according to a regular lattice. Intermediate configurations are possible, for instance in biological architectured materials, in which almost periodic structures or perturbed lattices are often encountered [7].

In addition, and beyond simply sparing matter, the creation of an inner architecture opens up new possibilities for designing multifunctional materials. This design is halfway between **material design and structure engineering**, indeed length scales, composition and geometry are controllable at the same scale [7, 9].

If the organisation of the matter at intermediate scales paves the way for new possibilities [5, 10, 15], it also poses new challenges in modelling and simulation. Indeed, due to the complex internal geometry of architectured materials, Direct Numerical Simulations (DNS, i.e. when the geometry of the inner structure is explicitly meshed in simulations) are often limited to few unit cells, or few Representative Volume Elements (RVEs). In other words, the full-field computation of a structure made out of an architectured material can be prohibitively expensive, especially in the design phase in which the structure is optimized.

To solve these technical difficulties, a possible way is to substitute the actual material by a homogeneous one having *equivalent* effective properties.

In the context of linear elasticity, to which this paper sticks to[1], the goal is to define the apparent fourth-order elasticity tensor $\underset{\approx}{\mathrm{C}}^{\star}$ which, over a RVE, relates the second-order volume-average strain tensor $(\underset{\sim}{\mathrm{E}})$ to the second order volume-average stress tensor $(\underset{\sim}{\Sigma})$:

$$\underset{\approx}{\mathrm{C}}^{\star} : \underset{\sim}{\mathrm{E}} = \underset{\sim}{\Sigma}$$

The averaged strain and stress tensors are defined over the domain Ω from the local fields $\underset{\sim}{\varepsilon}(\underline{\mathrm{x}})$, $\underset{\sim}{\sigma}(\underline{\mathrm{x}})$:

$$\underset{\sim}{\mathrm{E}} = \langle \underset{\sim}{\varepsilon}(\underline{\mathrm{x}}) \rangle = \frac{1}{V} \int_{\Omega} \underset{\sim}{\varepsilon}(\underline{\mathrm{x}}) \ \mathrm{d}V \qquad ; \qquad \underset{\sim}{\Sigma} = \langle \underset{\sim}{\sigma}(\underline{\mathrm{x}}) \rangle$$

with V the volume of Ω.

This approach is particularly useful for material and structure optimiza-

[1] **To avoid any misunderstanding, the approach we follow here is not restricted to linear elasticity and can be extended to more general constitutive behaviours such as: finite elasticity, viscoelasticity, plasticity,...**

tion, in which the model needs to be evaluated a numerous amount of times. The use of a homogenized approach makes it possible to localize "quickly" the vicinity of an optimal solution. In this neighborhood, the return to a more detailed model can become relevant again [11, 27].

The recent development of additive manufacturing techniques induces a gain of interest in the field of architected materials. Intricate inner structures that were, up to recently, restrained to theoretical discussions can now be produced and tested [23]. However, despite important progresses that have recently been made, the material state and the geometric characteristic obtained by those techniques remain poor and variable according to the printing technique [21, 33], the characteristics of the machine [6], **the heating energy strategy [25, 36]**, the orientation [35] and even the position on the printing table [35].

These disparities not only affect the elastic properties of the produced structures, but also their life expectancy.

Hence, in order to fully characterize a sample of architectured material the numerical studies have to be supplemented by experimental testings. But these testings are not standard since what has to be measure is not the behaviour of a constitutive material, but the effective elasticity of an architectured material.

If homogenization is a well-known topic both in theoretical and numerical mechanics [16], its experimental counterpart has to be built. It is worth being noted that if many homogenization procedures are available in the literature [24, 14, 8, 3, 30], few of them can be adapted to an experimental setting. For instance, if applying complex volume loadings, and full-field measurements of displacement field are heavy to carry out but feasible, direct stress measurement is not possible. Further, the approaches requiring too complex mechanical loads or accessing too much information can not be envisaged with a reasonable cost. The strategies which seem the most likely to be adapted to the experimental framework are those based on the control of boundary conditions. Those approaches are known, in the field of numerical homogenization, as Kinematic Uniform Boundary Conditions (KUBC) and Static Uniform Boundary Conditions (SUBC) or Periodic Boundary Conditions (PBC) [18, 8]. The last one is maybe the more appealing since PBC provides exact results [24, 8], however they are not simple to apply in practice. Uniform boundary conditions are simpler to use, but they rather measure apparent properties of the sample instead of effective properties of the considered material, KUBC overestimating overall rigidity while SUBC underestimating it [18, 19, 29, 17]. The result depends on the number of unit cells in the sample, but converges while increasing the number of unit cells to the effective properties of the architectured material [22]. Hence, to ensure

that the measured properties are those of the architectured material (effective properties) and not of the structure (apparent properties), a preliminary convergence study is required to size the sample to be tested.

The step-by-step transition from a perfectly theoretical situation to an amenable one for experimental testing is depicted in the diagram Figure 1 where going from one step to another step implies the weakening of a hypothesis.

All along this paper, plane strain will be be assumed, and the approach is hence mostly bidimensionnal. When required, assumptions justifying this hypothesis will be indicated in the core of the text.

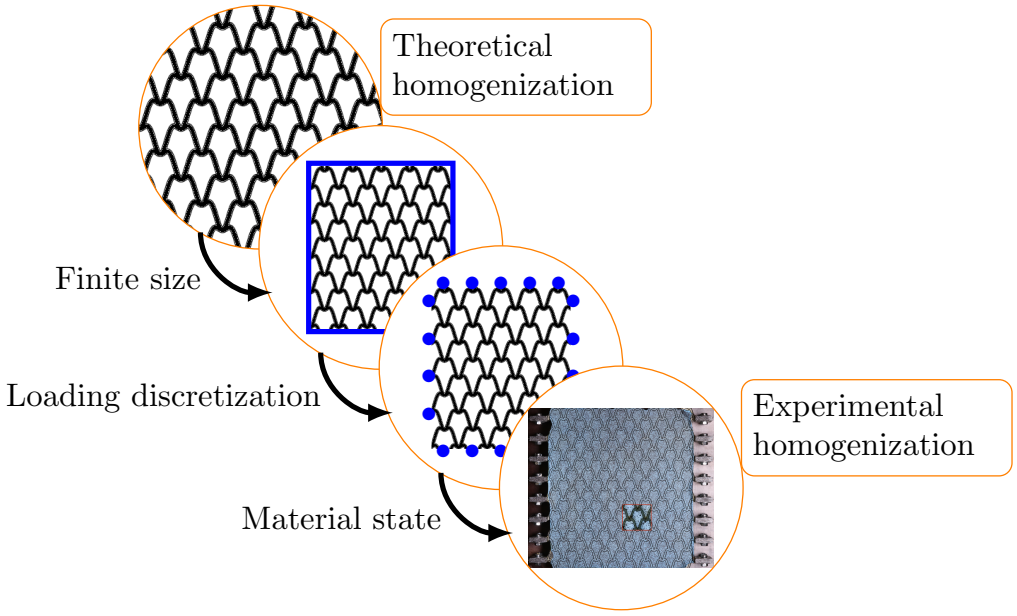

Figure 1: Step-by-step transition from a perfectly theoretical situation to an amenable one for experimental testing.

The aim of the present paper is thus to investigate the technological feasibility of such a transition from theoretical homogenization to an experimental rig. As mentioned before, this transition will be here considered in the context of linear elasticity. Needless to say that the development of an experimental system capable of applying complex boundary conditions can find applications broader than **homogenization of linear elasticity of composites. First it can be used for the homogenization of more complex behavior, like viscoelasticity and elastoplasticity. We believe, for instance, that the device we set up will be of great interested for understanding the anisotropic viscoelastic proper-**

ties of (real) architectured materials. This question is of prime importance for the modelling of polymer architectured materials (such as the one obtained by 3D printers), or for biological materials. Second, and for non-linear materials, it can be used to study the change in their effective properties when strained (e.g. acoustoelasticity). Last, it can be used to study the evolution of local phenomena, like instabilities or crack propagations, when the embedded material is submitted to a remote biaxial strain/stress state (a sort of Experimental Eshelby Problem).[2]

The paper is organized as follows: first, in section 2, the description of the problem and the principle of **the homogenization by KUBC or SUBC is explained. This leads to the question of the technical possibility of a mechanical system able to perform KUBC, or SUBC, or both**. For simplicity's sake, the route of displacement controlled experiments is followed, leaving aside the study of the feasibility of a SUBC system for forthcoming investigations. By the end of this section the important question of the measurement of the average stress in the sample is asked and solved. It opens the way for studying the technological aspects of the mechanism in section 3, and a candidate architecture for the testing device is proposed. In section 4, a Virtual Testing Device (VTD in the following) based on the choices previously made is implemented. The aim of the VTD is to validate the operating principle of the considered device architecture, optimize its design and evaluate its capabilities. Hence, after describing aspects of its numerical implementation, the VTD is ultimately validated on some elementary simulations representing critical testing situations. Finally, some general conclusions and perspectives are given in section 5.

1.2. Notations

Space and basis:

Throughout this paper, the physical space is modelled on the Euclidean space $\mathcal{E}^2$ with E^2 its associated vector space. Once an arbitrary reference point is chosen, those spaces can be associated and $\mathcal{P} = \{\underline{e}_1, \underline{e}_2\}$ will denote an orthonormal basis of E^2. When needed tensor components are specified with respect to $\mathcal{P}$.

[2] **The context of homogenization in linear elasticity is interesting for designing a machine since the theoretical framework is clear and well-understood, for instance, 1) the control parameters are clearly identified as the quantities to measure for reconstructing the overall behaviour, 2) analytical/numerical solution to validate the design of the machine are easy to obtain.**

For forthcoming needs, let also defined $\mathcal{M} = \{\underline{\hat{e}}_1, \underline{\hat{e}}_2, \underline{\hat{e}}_3\}$ the orthonormal canonical basis of $\mathbb{R}^3$, in the present context $\mathcal{M}$ will be referred to as the Mandel basis. Vectors of $\mathcal{M}$ are obtained from second orders tensors of $\mathcal{P}$ according to the following construction. Consider the following linear application $\phi : S^2(\mathbb{R}^2) \to \mathbb{R}^3$:

$$\begin{aligned} \underline{\hat{e}}_1 &= \phi(\underline{e}_1 \otimes \underline{e}_1), \\ \underline{\hat{e}}_2 &= \phi(\underline{e}_2 \otimes \underline{e}_2), \\ \underline{\hat{e}}_3 &= \phi(\frac{\sqrt{2}}{2}(\underline{e}_1 \otimes \underline{e}_2 + \underline{e}_2 \otimes \underline{e}_1)). \end{aligned} \tag{1}$$

With respect to $\mathcal{M}$, we can define the vector $\underline{\hat{t}}$ image of $\underset{\sim}{t}$ by ϕ.

Tensor products:

Tensors of order 0, 1, 2 and 4 are denoted respectively by $\cdot$, $\underline{\cdot}$, $\underset{\sim}{\cdot}$, $\underset{\approx}{\cdot}$. The matrix expression of the quantity $(\cdot)$ in the basis β is symbolized by $[\cdot]_\beta$. The simple, double and fourth-order contractions are written $\cdot$, :, :: respectively. In components, with respect to $\mathcal{P}$, these notations correspond to

$$\underline{u} \cdot \underline{v} = u_i v_i \qquad \underset{\sim}{a} : \underset{\sim}{b} = a_{ij} b_{ij}$$
$$(\underset{\approx}{A} : \underset{\approx}{B})_{ijkl} = A_{ijpq} B_{pqkl} \qquad (\underset{\approx}{A} :: \underset{\approx}{B}) = A_{pqrs} B_{pqrs}$$

where the Einstein summation on repeated indices is used. The order on which components are summed has been chosen in such a way that the full contraction between same order tensors is a scalar product. $\otimes$ stands for the classical product.

Miscellaneous notations:

- $[\underline{\nabla}]_{\mathcal{P}} = \frac{\partial}{\partial x_i} \underline{e}_i$ the nabla operator;
- $\partial_K \Omega$ the restriction of $\partial\Omega$ on which kinematic conditions are imposed;
- $\partial_S \Omega$ the restriction of $\partial\Omega$ on which static conditions are imposed;
- $\overline{(\cdot)}$ imposed quantity;
- $[\![\cdot]\!]$ the jump of $(\cdot)$.

2. Transposition of an homogenisation scheme ...

In this section, a methodology for determining the apparent elastic behaviour of a sample of architectured material with an experimental setup is exposed. First, the mechanical problem is defined. Next, an equivalence criterion between micro and macro scales is made explicit, which leads to the choice of a homogenisation scheme which will then be detailed. The end of this section is devoted to proposing technological solutions to transpose this scheme into an experimental context.

2.1. Description of the sample

The sample of the architectured material we intent to determine the homogenized behaviour of is supposed to occupy a bounded domain Ω of $\mathbb{R}^2$ with boundary denoted by $\partial\Omega$ (fig 2) and $\overline{\Omega}$ it's closure. Points within Ω will be referred to as material points and, upon the choice of a spatial reference point O defining $\mathcal{R}$ a frame of reference of E^2, material points can be designated by their position vector $\underline{\mathrm{x}}$ within $\mathcal{R}$.

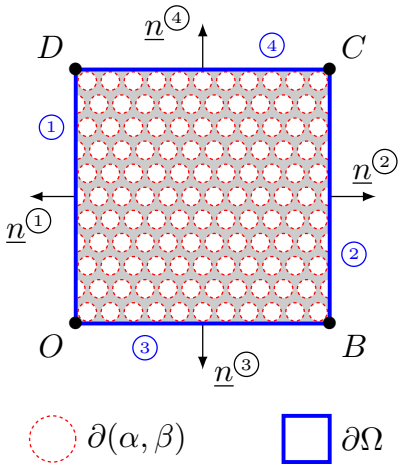

Figure 2: Definition of the considered domain Ω

O is taken at the bottom left corner, position and normal vector on the boundary are defined in table 1.

Ω is supposed to be filled by two elastic materials thereafter referred to as phase α and β. The boundary between the phases is symbolized by $\partial(\alpha,\beta)$. Let's denote by L, l and λ the characteristic lengths of the macrostructure, mesostructure and microstructure respectively (fig 3). The microstructure and its characteristic length λ is assumed to be well separated with respect

edge	①	②	③	④
$\underline{n}$	$\begin{pmatrix}-1\\0\end{pmatrix}$	$\begin{pmatrix}1\\0\end{pmatrix}$	$\begin{pmatrix}0\\-1\end{pmatrix}$	$\begin{pmatrix}0\\1\end{pmatrix}$
$\underline{x}$	$\begin{pmatrix}0\\y\end{pmatrix}$	$\begin{pmatrix}L\\y\end{pmatrix}$	$\begin{pmatrix}x\\0\end{pmatrix}$	$\begin{pmatrix}x\\L\end{pmatrix}$

Table 1: Values of $\underline{n}$ and $\underline{x}$ on the different edges

to l, so, although intrinsically present in the real material, it will not be investigated. The scale separation ratio ϵ can thereby be defined:

$$\epsilon = \frac{l}{L}$$

The scales are said separated when $\epsilon \to 0$, which is the situation of classical homogenization.

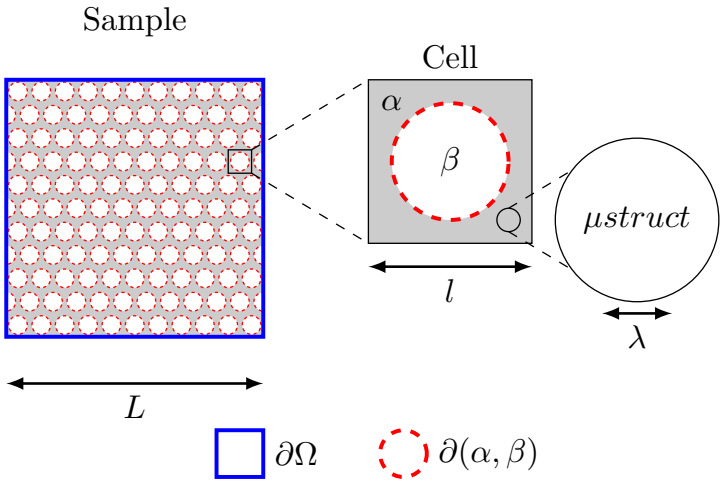

Figure 3: Characteristic length scales of the mechanical problem

The physical properties of those elastic phases are supposed to be defined by two, possibly anisotropic, elasticity tensors $\underset{\approx}{c}^{\alpha}$ and $\underset{\approx}{c}^{\beta}$. The elasticity tensor at a given point $\underline{x}$ of Ω is described by the function:

$$\underset{\approx}{c}(\underline{x}) = \chi(\underline{x})\underset{\approx}{c}^{\alpha} + (1 - \chi(\underline{x}))\underset{\approx}{c}^{\beta}$$

in which χ denotes the characteristic function of phase α, i.e.

$$\chi(\underline{x}) := \begin{cases} 1, & \text{if } \underline{x} \in \alpha \\ 0, & \text{if } \underline{x} \notin \alpha \end{cases}$$

In classical homogenization, $\underset{\approx}{c}$ must be positive definite. However, for our needs we will allow ourselves

$$\underset{\approx}{c}^{\beta} \to 0$$

in order to represent pores. This situation belongs to the category of high contrast homogenization [1]. This hypothesis might present theoretical and numerical problems, indeed the homogenized properties depend on the way the asymptotic method is conducted ([1]) and [34] show that non local effect can be obtained. However none of these should be a problem in the case of experimental homogenization. No body forces are considered. Hence the local equations for a pure Dirichlet problem are:

$$\begin{cases} \underline{\nabla} \cdot (\underset{\approx}{c}(\underline{x}) : \underset{\sim}{\varepsilon}(\underline{x})) = \underline{0}, & \text{for } \underline{x} \in \ \Omega \\ [\![\underset{\sim}{\sigma}(\underline{x}) \cdot \underline{n}]\!] = \underline{0}, & \text{for } \underline{x} \in \partial(\alpha, \beta) \\ \underline{u} = \overline{\underline{u}} & \text{on } \partial\Omega \end{cases}$$

with the kinematic compatibility condition[3]:

$$\underset{\sim}{\varepsilon}(\underline{x}) = \frac{1}{2} \left(\underline{u}(\underline{x}) \otimes \underline{\nabla} + \underline{\nabla} \otimes \underline{u}(\underline{x}) \right), \quad \text{for } \underline{x} \text{ in } \Omega$$

2.2. Hill-Mandel condition

Before the homogenization process the considered material is heterogeneous and the fields vary locally with the heterogeneities. After the homogenization process it is replaced by a homogeneous one and the fields vary globally. It is important to define an equivalence between these two descriptions of the same medium. Different equivalence criteria are possible, among

[3] **All the equations are provided here under the assumption that $\|\underline{u}(\underline{x}) \otimes \underline{\nabla}\| \ll 1$. This hypothesis makes it possible to confound the initial and distorted configurations, and to bring the equilibrium study on the initial configuration. This hypothesis, which is legitimate in view of the applications considered in this paper, can nevertheless be weakened, and the equations adapted accordingly.**

which the Hill-Mandel energy criterion is chosen [18]:

$$\langle \underset{\sim}{\sigma}(\underline{x}) : \underset{\sim}{\varepsilon}(\underline{x}) \rangle = \underset{\sim}{\Sigma} : \underset{\sim}{E} \tag{2}$$

Let's denote by $KA(\Omega)$ the set of kinematically admissible displacement fields over Ω and by $SA(\Omega)$ the set of statically admissible stress fields over Ω. Neither body force, nor rigid body motion are considered.

$$\begin{cases} KA(\Omega) & = \{ \underline{u}' \mid \underline{u}'(\underline{x}) = \underline{\overline{u}}(\underline{x}),\ \forall \underline{x} \in \partial_K \Omega \} \\ SA(\Omega) & = \left\{ \underset{\sim}{\sigma}' \mid \underline{\nabla} \cdot \underset{\sim}{\sigma}'(\underline{x}) = \underline{0},\ \forall \underline{x} \in \Omega \ ||\ \underset{\sim}{\sigma}'(\underline{x}) \cdot \underline{n} = \underline{\bar{t}}(\underline{x}),\ \forall \underline{x} \in \partial_S \Omega \right\} \end{cases}$$

$\underline{\overline{u}}(\underline{x})$ and $\underline{\bar{t}}(\underline{x})$ being the kinematic and static boundary conditions applied on $\partial_K \Omega$ and $\partial_S \Omega$ respectively. Considering $\underline{u}'(\underline{x})$, $\underset{\sim}{\varepsilon}'(\underline{x})$ and $\underset{\sim}{\sigma}'(\underline{x})$ such as:

$$\begin{cases} \underset{\sim}{\varepsilon}'(\underline{x}) = \dfrac{1}{2} \left(\underline{u}'(\underline{x}) \otimes \underline{\nabla} + \underline{\nabla} \otimes \underline{u}'(\underline{x}) \right), & \text{with } \underline{u}' \in KA(\Omega) \\ \underset{\sim}{\sigma}'(\underline{x}) \in SA(\Omega) \end{cases}$$

By extension a strain field will be said KA if it is the symmetrised gradient of a displacement $\underline{u}' \in KA(\Omega)$. In such case and with a slight abuse of notation, we will note $\underset{\sim}{\varepsilon}' \in KA(\Omega)$.

For any $\underline{u}', \underset{\sim}{\sigma}' \in KA \times SA$ the following quantities can be defined:

$$\begin{cases} \underset{\sim}{\Sigma}' & = \langle \underset{\sim}{\sigma}'(\underline{x}) \rangle \\ \underset{\sim}{E}' & = \langle \underset{\sim}{\varepsilon}'(\underline{x}) \rangle \\ \underline{U}' & = \underset{\sim}{E}' \cdot \underline{x} \end{cases} \quad \Rightarrow \quad \begin{cases} \underset{\sim}{\delta\sigma}'(\underline{x}) & = \underset{\sim}{\sigma}'(\underline{x}) - \underset{\sim}{\Sigma}' \\ \underset{\sim}{\delta\varepsilon}'(\underline{x}) & = \underset{\sim}{\varepsilon}'(\underline{x}) - \underset{\sim}{E}' \\ \underline{\delta u}'(\underline{x}) & = \underline{u}'(\underline{x}) - \underline{U}' \end{cases}$$

in which $\underline{U}'$ is the average displacement field, while $\underline{\delta u}'$, $\underset{\sim}{\delta\varepsilon}'$ and $\underset{\sim}{\delta\sigma}'$ are, respectively, the displacement, strain and stress fluctuations around the means. In this analysis, **it is not necessary to make the assumption of a given constitutive model linking $\underset{\sim}{\sigma}'$ and $\underset{\sim}{\varepsilon}'$ (*e.g.* a linear relationship due to elasticity)**.

The mechanical energy associated to these fluctuations has the following expression:

$$\langle \underset{\sim}{\delta\sigma}'(\underline{x}) : \underset{\sim}{\delta\varepsilon}'(\underline{x}) \rangle = \langle \underset{\sim}{\sigma}'(\underline{x}) : \underset{\sim}{\varepsilon}'(\underline{x}) \rangle - \underset{\sim}{\Sigma}' : \underset{\sim}{E}'$$

Complying with Hill-Mandel condition (eq (2)) amounts to have a null average work of the fluctuations.

Since

$$\delta\varepsilon'_{ij}(\underline{\mathrm{x}}) = \varepsilon'_{ij}(\underline{\mathrm{x}}) - E'_{ij} = \frac{1}{2}\left(\delta u'_{i,j}(\underline{\mathrm{x}}) + \delta u'_{j,i}(\underline{\mathrm{x}})\right)$$

and due to the symmetry of $\underset{\sim}{\delta\sigma'}$

$$\delta\sigma'_{ij}(\underline{\mathrm{x}})\ \delta u'_{i,j}(\underline{\mathrm{x}}) = \delta\sigma'_{ij}(\underline{\mathrm{x}})\ \delta u'_{j,i}(\underline{\mathrm{x}})$$

the work of the fluctuation can be expressed as:

$$\langle \underset{\sim}{\delta\sigma'}(\underline{\mathrm{x}}) : \underset{\sim}{\delta\varepsilon'}(\underline{\mathrm{x}})\rangle = \frac{1}{V}\int_\Omega \left(\delta\sigma'_{ij}(\underline{\mathrm{x}})\ \delta u'_i(\underline{\mathrm{x}})\right)_{,j}\ \mathrm{d}V - \int_\Omega \delta\sigma'_{ij,j}(\underline{\mathrm{x}})\ \delta u'_i(\underline{\mathrm{x}})\ \mathrm{d}V$$

The vanishing of body forces

$$\delta\sigma'_{ij,j}(\underline{\mathrm{x}}) = \underline{\nabla}\cdot\left[\underset{\sim}{\sigma'}(\underline{\mathrm{x}}) - \underset{\sim}{\Sigma'}\right] = 0$$

leads to

$$\langle \underset{\sim}{\delta\sigma'}(\underline{\mathrm{x}}) : \underset{\sim}{\delta\varepsilon'}(\underline{\mathrm{x}})\rangle = \frac{1}{V}\int_{\partial\Omega}\left(\underline{\mathrm{t}}(\underline{\mathrm{x}}) - \underset{\sim}{\Sigma'}\cdot\underline{\mathrm{n}}\right)\cdot\left(\underline{\mathrm{u}}'(\underline{\mathrm{x}}) - \underset{\sim}{\mathrm{E}'}\cdot\underline{\mathrm{x}}\right)\ \mathrm{d}S$$

So, among others, the following conditions satisfied eq (2):

$$\left|\begin{array}{ll} \underline{\mathrm{t}}(\underline{\mathrm{x}}) = \underset{\sim}{\Sigma}\cdot\underline{\mathrm{n}} & \forall\underline{\mathrm{x}}\in\partial\Omega \\ \underline{\mathrm{u}}(\underline{\mathrm{x}}) = \underset{\sim}{\mathrm{E}}\cdot\underline{\mathrm{x}} & \forall\underline{\mathrm{x}}\in\partial\Omega \end{array}\right. \tag{3}$$

with $\underset{\sim}{\Sigma}$ and $\underset{\sim}{\mathrm{E}}$ uniform.

The first set of Boundary Conditions in eq (3) is known as Static Uniform Boundary Conditions (SUBC) while the second defined Kinematic Uniform Boundary Conditions (KUBC) over Ω. These two boundary conditions ensure the Hill-Mandel criterion. In the rest of the article, only the method of homogenization by average fields in KUBC is studied.

2.3. Homogenization scheme

Fulfilling the homogenization of a linear elastic material by a KUBC method is looking for $\underset{\approx}{\mathrm{C}^\star}$ such as: $\underset{\sim}{\Sigma} = \underset{\approx}{\mathrm{C}^\star} : \underset{\sim}{\mathrm{E}}$. To introduce the method lets first consider the matrix expressions of $\underset{\sim}{\mathrm{E}}$ and $\underset{\sim}{\Sigma}$ in $\mathcal{P}$.

$$[\underset{\sim}{\mathrm{E}}] = \begin{pmatrix} E_{11} & E_{12} \\ E_{12} & E_{22} \end{pmatrix}_{\mathcal{P}} \qquad \text{and} \qquad [\underset{\sim}{\Sigma}] = \begin{pmatrix} \Sigma_{11} & \Sigma_{12} \\ \Sigma_{12} & \Sigma_{22} \end{pmatrix}_{\mathcal{P}}$$

Using Mandel transformation defined in section 1.2, these can be turned into vectors in $\mathbb{R}^3$:

$$[\hat{\underline{\mathrm{E}}}] = \begin{pmatrix} \hat{E}_1 = E_{11} \\ \hat{E}_2 = E_{22} \\ \hat{E}_3 = \sqrt{2}\, E_{12} \end{pmatrix}_{\mathcal{M}} \quad ; \quad [\hat{\underline{\Sigma}}] = \begin{pmatrix} \hat{\Sigma}_1 = \Sigma_{11} \\ \hat{\Sigma}_2 = \Sigma_{22} \\ \hat{\Sigma}_3 = \sqrt{2}\, \Sigma_{12} \end{pmatrix}_{\mathcal{M}}$$

The principle of mean field homogenization is as follows. Consider a mean state of strain $\hat{\underline{\mathrm{E}}}$ and stress $\hat{\underline{\Sigma}}$ over Ω, and decompose them on $\mathcal{M}$

$$\hat{\underline{\mathrm{E}}} = \hat{E}_i \hat{\underline{\mathrm{e}}}_i \quad , \quad \hat{\underline{\Sigma}} = \hat{\Sigma}_i \hat{\underline{\mathrm{e}}}_i$$

Suppose that $\hat{\underline{\Sigma}}$ is related to $\hat{\underline{\mathrm{E}}}$ by a linear relationship, that is by a constant positive definite fourth-order elasticity tensor $\hat{\underset{\sim}{\mathrm{C}}}$

$$[\hat{\underset{\sim}{\mathrm{C}}}] = \begin{pmatrix} C_{1111} & C_{1122} & \sqrt{2}C_{1112} \\ C_{1122} & C_{2222} & \sqrt{2}C_{2212} \\ \sqrt{2}C_{1211} & \sqrt{2}C_{1222} & 2C_{1212} \end{pmatrix}_{\mathcal{M}} = \begin{pmatrix} \hat{C}_{11} & \hat{C}_{12} & \hat{C}_{13} \\ \hat{C}_{12} & \hat{C}_{22} & \hat{C}_{23} \\ \hat{C}_{13} & \hat{C}_{23} & \hat{C}_{33} \end{pmatrix}_{\mathcal{M}}$$

By mean of linearity, $\hat{\underline{\Sigma}}$ can be written

$$\hat{\underline{\Sigma}} = \hat{\underset{\sim}{\mathrm{C}}} \cdot \hat{\underline{\mathrm{E}}} = \hat{E}_i \hat{\underline{\Sigma}}^{\mathbb{1}}_i, \quad \text{with} \quad \hat{\underline{\Sigma}}^{\mathbb{1}}_i = \hat{\underset{\sim}{\mathrm{C}}} \cdot \hat{\underline{\mathrm{e}}}_i$$

in which $\hat{\underline{\Sigma}}^{\mathbb{1}}_i$ denotes the mean stress field associated to the unit strain field $\hat{\underline{\mathrm{e}}}_i$. This amounts to decompose $\hat{\underline{\Sigma}}$ over $\{\hat{\underline{\Sigma}}^{\mathbb{1}}_i\}_{1 \leq i \leq 3}$, which is a base of $\mathbb{R}^3$ due to the positive definiteness assumption. Thus

$$\hat{\underline{\Sigma}} = \hat{\Sigma}_j \hat{\underline{\mathrm{e}}}_j = \hat{E}_j \hat{\underline{\Sigma}}^{\mathbb{1}}_j$$

Hence

$$\hat{\Sigma}_i = \hat{\underline{\Sigma}} \cdot \hat{\underline{\mathrm{e}}}_i = \hat{E}_j \hat{\underline{\Sigma}}^{\mathbb{1}}_j \cdot \hat{\underline{\mathrm{e}}}_i$$

which means that

$$\hat{C}_{ij} = \hat{\underline{\mathrm{e}}}_i \cdot \hat{\underline{\Sigma}}^{\mathbb{1}}_j$$

or, more explicitly

$$[\hat{\underset{\sim}{\mathrm{C}}}] = \begin{pmatrix} \hat{\underline{\Sigma}}^{\mathbb{1}}_1 \cdot \hat{\underline{\mathrm{e}}}_1 & \hat{\underline{\Sigma}}^{\mathbb{1}}_2 \cdot \hat{\underline{\mathrm{e}}}_1 & \hat{\underline{\Sigma}}^{\mathbb{1}}_3 \cdot \hat{\underline{\mathrm{e}}}_1 \\ \hat{\underline{\Sigma}}^{\mathbb{1}}_1 \cdot \hat{\underline{\mathrm{e}}}_2 & \hat{\underline{\Sigma}}^{\mathbb{1}}_2 \cdot \hat{\underline{\mathrm{e}}}_2 & \hat{\underline{\Sigma}}^{\mathbb{1}}_3 \cdot \hat{\underline{\mathrm{e}}}_2 \\ \hat{\underline{\Sigma}}^{\mathbb{1}}_1 \cdot \hat{\underline{\mathrm{e}}}_3 & \hat{\underline{\Sigma}}^{\mathbb{1}}_2 \cdot \hat{\underline{\mathrm{e}}}_3 & \hat{\underline{\Sigma}}^{\mathbb{1}}_3 \cdot \hat{\underline{\mathrm{e}}}_3 \end{pmatrix}_{\mathcal{M}} \tag{4}$$

Hence the theoretical determination of a column of $[\hat{\underset{\sim}{\mathrm{C}}}]$ is a three-step

process:

1. imposing a mean strain state $\underline{\hat{e}}_i$ over Ω;
2. measuring the resulting stress field $\underline{\hat{\sigma}}^{\mathbb{1}}(\underline{x})$;
3. computing the average stress field $\underline{\hat{\Sigma}}^{\mathbb{1}}$ and the associated dot products.

So, the application of a KUBC homogenization approach in an experimental setting presents two main difficulties:

- applying kinematic uniform boundary conditions on a sample;
- determining the value of the macroscopic stress $\underset{\sim}{\Sigma}$.

The end of this section is devoted to proposing solutions to these complications. First the global concept of a device capable of applying KUBC is discussed. Then, a method to compute the average stress field in an experimental setting with realistic measuring means is presented.

2.4. Machine type

Up to authors best knowledge, no machine designed for imposing KUBC have been studied, or designed yet. It is therefore necessary to conceive one (almost) from scratch. Theoretically KUBC are continuous, and a fine discretization is mandatory to perform corresponding numerical simulations. However experimentally, continuous conditions might be hard to obtain, and thereby, will not be searched at all costs.

In a practical way, architectured materials will be tested so that edges will be divided into several subsets corresponding to the various constituents and/or to the voids. The sample will be fastened to the testing device through its most rigid phase. The number of rigid subsets on the boundary is directly linked to the number of cells in the sample (fig 4). In order to achieve a good scale separation for the architectured material ($\epsilon \to 0$), a minimum of 10 cells along each dimension is required [28]. Here, one will only investigate the Cauchy-elasticity so that this condition must be satisfied otherwise overall classical elasticity may no longer be sufficient to describe the static behaviour of the material [2, 26]. Thus we will consider a square sample with 10 rigid subsets on each edge. Each surface will be mechanically fastened and assimilated to a control point or a lattice node with 2 degrees of freedom (dof).

Two types of machines with multiple control points are conceivable (Figure 4): local type, with independent control points; or global type, with

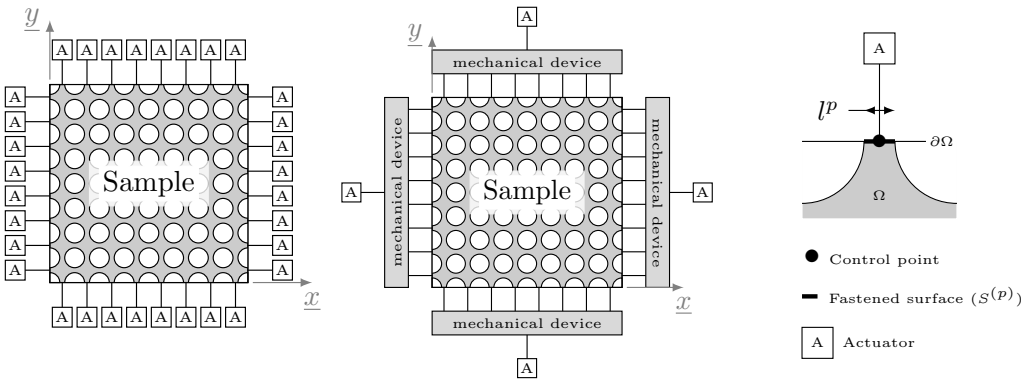

(a) Local type machine (b) Global type machine (c) Local description

Figure 4: Schematic diagram of local and global type devices

related ones. A few examples of both types are found in the literature (e.g. [12] and [32]) for local type; [20] and Accupull© device for global type). The pros and the cons related to each option will be discussed.

2.4.1. Local type

The idea of this approach is to independently command each control point using as many actuators as necessary: one or more per point depending on the desired kinematics. In our case, which involves 10 control points with 2 dof on 4 edges, this represents 80 actuators. This type of machine allows to apply any discretized KUBC or SUBC and to measure the dual quantity on the boundary of the specimen. With such a configuration, all the information necessary to the homogenization scheme is measurable.

The cost of such a system is roughly equivalent to the cost of a global type one (numerous actuators and parts on one side, less actuators but more parts on the other). However, having a large number of actuators also presents technical problems. To a small extent, controlling simultaneously and precisely eighty actuators is possible but requires a lot of equipment. But the main problem is bulkiness. Indeed, for the considered size and load range it is hard to find matching actuators. These two problems are accentuated by the addition of load cells.

2.4.2. Global type

The idea of this approach is to have a limited number of actuators and a mechanical device between them and the specimen that carry out the repartition of the displacement or force over the different control points. If one imposes load on the boundary, a kinematic measurement has to be taken.

Conversely if one imposes a displacement to the boundary, load cells will be necessary on each dof to know the load repartition and the same difficulties as before would appear.

This approach requires to control less actuators but the error of each control point due to the machine defects can not be corrected by compensating the command send to the common actuator. A global force or displacement measurement is conceivable but it might not be possible to achieve a homogenization scheme with so little information.

The two approaches seems reasonable and both have strengths and weaknesses, but the global one seems more elegant to our eyes. Only this idea will be considered thereafter.

2.5. Feasibility of the experimental homogenization

Before going further, it is necessary to ensure the feasibility of determining the average stress state by realistic experimental means. Indeed, the field $\underline{\hat{\sigma}}(\underline{\mathrm{x}})$ has to be known and if this is easy to achieve in a numerical situation, generally speaking this information is not measurable in an experimental setting. It has therefore to be determined with information poorer than the knowledge of the field in every point. As it will be shown, this is however possible by making some assumptions.
First, the average operation can be projected on the edges:

$$\begin{aligned} V\underset{\sim}{\Sigma} &= \int_\Omega \sigma_{ij}\ \mathrm{d}V = \int_\Omega \sigma_{ik}\delta_{kj}\ \mathrm{d}V = \int_\Omega \sigma_{ik}x_{j,k}\ \mathrm{d}V \\ &= \int_\Omega (\sigma_{ik}x_j)_{,k}\ \mathrm{d}V - \int_\Omega \sigma_{ik,k}x_j\ \mathrm{d}V \\ &= \int_{\partial\Omega} (\underset{\sim}{\sigma}\cdot\underline{\mathrm{n}})\otimes\underline{\mathrm{x}}\ \mathrm{d}S \end{aligned}$$

Because of the absence of body force, $\underline{\nabla}\cdot\underset{\sim}{\sigma}$ in the former relation vanishes, while the first one is transformed into a surface integral according to the divergence theorem. In our case, the boundary $\partial\Omega$ is divided into 2 subsets corresponding to the two phases: material and void (stress free) (fig 4). The material subset is divided into several fastened surfaces. So the integral can be split as follows with $4N$ the number of fasteners on $\partial\Omega$ and $\partial\Omega^{(p)}$ the restriction of $\partial\Omega$ to one fastener:

$$V\underset{\sim}{\Sigma} = \sum_{p=1}^{4N}\int_{\partial\Omega^{(p)}} \left(\underset{\sim}{\sigma}^{(p)}\cdot\underline{\mathrm{n}}^{(p)}\right)\otimes\underline{\mathrm{x}}\ \mathrm{d}S \tag{5}$$

in which $(\,\cdot\,)^{(p)}$ denotes the restriction of $(\,\cdot\,)$ to $\partial\Omega^{(p)}$.

Now supposing that the fasteners are sufficiently narrow so that the fields are locally linear:

$$\underset{\sim}{\sigma}^{(p)}(\underline{\mathrm{x}}) \simeq \underset{\sim}{\sigma}^{0(p)} + \left(\underline{\mathrm{y}}^{(p)}(\underline{\mathrm{x}}) \cdot \underline{\mathrm{e}}^{(p)}\right) \underset{\sim}{\sigma}^{1(p)}$$

with $\underset{\sim}{\sigma}^{0(p)}$ and $\underset{\sim}{\sigma}^{1(p)}$ two constant tensors while $\underline{\mathrm{y}}^{(p)}$ and $\underline{\mathrm{e}}^{(p)}$ are the local position vector and the basis vector collinear to the edge, respectively:

$$\underline{\mathrm{y}}^{(p)} = \underline{\mathrm{x}} - \underline{\mathrm{x}}^{(p)}$$

In this last expression $\underline{\mathrm{x}}^{(p)}$ represents the center of the fastener (p), that is the control point on fig 4c.

Starting from eq (5), and after some algebra **detailed in** Appendix A, the following expression for the average stress is obtained:

$$V \underset{\sim}{\Sigma} = \sum_{p=1}^{4\,N} L\, S^{(p)} \left[\left(\underset{\sim}{\sigma}^{0(p)} \cdot \underline{\mathrm{n}}^{(p)} \right) \otimes \frac{\underline{\mathrm{x}}^{(p)}}{L} + \frac{1}{12} \left(l^{(p)}\, \underset{\sim}{\sigma}^{1(p)} \cdot \underline{\mathrm{n}}^{(p)} \right) \frac{l^{(p)}}{L} \right]$$

in which $S^{(p)} = l^{(p)}\, H$ is the surface of a fastener ($l^{(p)}$ being its width and H the sample out-of-plane thickness), and L is the length of a side of the specimen. The first term corresponds to the mean value of the stress over a fastener while the second corresponds to a first order approximation for the variation of the stress. On can now compare the order of magnitudes of these two contributions:

$$\begin{cases} O\left(\dfrac{\mathrm{x}_j^{(p)}}{L}\right) = 1 \quad ; \quad \text{inherently} \\[2ex] O\left(\dfrac{l^{(p)}}{L}\right) = 10^{-2} \quad ; \quad \text{by hypothesis} \end{cases}$$

The order of magnitude of the second term vary with $\frac{l^{(p)}}{L}$, $l^{(p)}$ being the in-plane size of the fasteners, which are very narrow by hypothesis. As a consequence the second term can be neglected with regard to the first and will not be considered afterwards. Our assumption leads ultimately to:

$$V \underset{\sim}{\Sigma} = \sum_{p=1}^{4N} S^{(p)} \left(\underset{\sim}{\sigma}^{0(p)} \cdot \underline{\mathrm{n}}^{(p)} \right) \otimes \underline{\mathrm{x}}^{(p)} \tag{6}$$

We then split down the previous sum (eq (6)) on all four edges.

$$V\underset{\sim}{\Sigma} = \sum_{s=1}^{4}\sum_{p=1}^{N} S^{(sp)}\left(\underset{\sim}{\sigma}^{(sp)}\cdot\underline{\mathrm{n}}^{(s)}\right)\otimes\underline{\mathrm{x}}^{(sp)}$$

Or, in matrix form:

$$V\underset{\sim}{\Sigma} = \begin{pmatrix} \sum_{p=1}^{N}\left(L\,f_x^{(2p)} - x^{(3p)}\,f_x^{(3p)} + x^{(4p)}\,f_x^{(4p)}\right) & \sum_{p=1}^{N}\left(-y^{(1p)}\,f_x^{(1p)} + y^{(2p)}\,f_x^{(2p)} + L\,f_x^{(4p)}\right) \\ \sum_{p=1}^{N}\left(L\,f_y^{(2p)} - x^{(3p)}\,f_y^{(3p)} + x^{(4p)}\,f_y^{(4p)}\right) & \sum_{p=1}^{N}\left(-y^{(1p)}\,f_y^{(1p)} + y^{(2p)}\,f_y^{(2p)} + L\,f_y^{(4p)}\right) \end{pmatrix}_{\mathcal{P}} \tag{7}$$

in which $f_j^{(sp)} = S^{(sp)}\,\sigma_{jk}^{(sp)}\,n_k^{(s)}$ the j-th component of the force on the (p)-th fastener of the edge (s). The expression of $\underset{\sim}{\Sigma}$ obtained here is not symmetrical following the projections because of the choice of the origin on a corner of the domain. However, when determining the experimental values, a symmetric expression is expected.

The value of these sums remains to be determined. The terms contributing to the overall stress are of two kinds:

$$\begin{cases} \displaystyle\sum_{p=1}^{N} L\,f_j^{(sp)} = L\,F_j^{(s)}, & j=\{x,y\},\ s=[1;4] \\ \displaystyle\sum_{p=1}^{N} X^{(sp)}\,f_j^{(sp)}, & X=\{x,y\},\ j=\{x,y\},\ s=[1;4] \end{cases}$$

The first is easy to compute in an experimental setting since the information provided by the measurement of the global forces on one edge is sufficient. At first glance, the computation of the terms of the second kind requires the implementation of force sensors on each of the fasteners. However for cost and bulkiness reasons it is best, if possible, to avoid this addition. To determine this sum more simply, consider the equilibrium of the mechanical device associated with one of the edges. The case of edge ① ($s=1$) is represented and analyzed below, the other cases being similar.

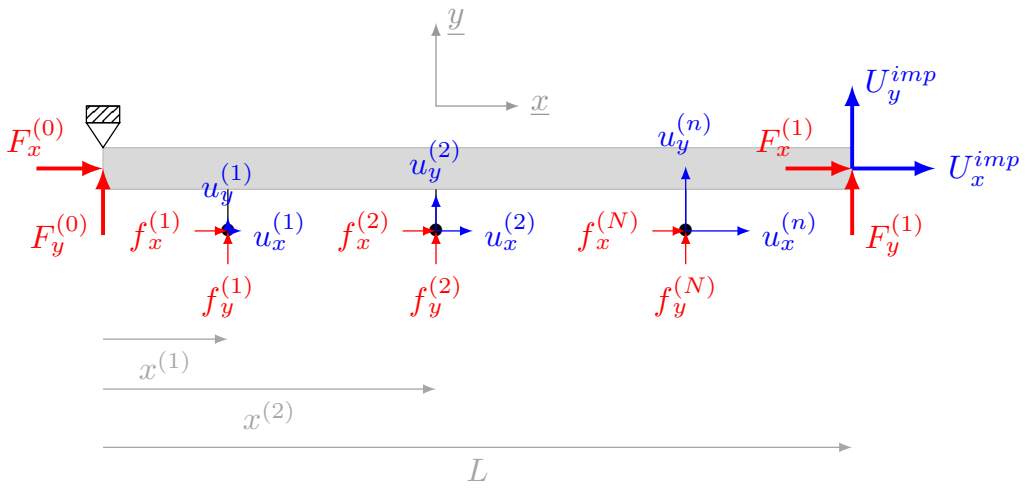

Figure 5: Equilibrium of the mechanical device associated to one of the edges

Once again, two cases emerge

1. the forces on the device are orthogonal to the medium line of the application device $f_y^{(p)}$, $p \in [\![1; N]\!]$ on fig 5;
2. the forces on the device are collinear to the medium line of the application device $f_x^{(p)}$, $p \in [\![1; N]\!]$ on fig 5.

Everything being considered linear, they can be solved separately.

1. In the first case $\sum_{p=1}^{N} x^{(p)}\, f_y^{(p)}$ is simply given by the angular momentum equation of the static equilibrium:

$$\sum_{p=1}^{N} x^{(p)}\, f_y^{(p)} = F_y^{(1)}\, L \tag{8}$$

2. In the second case, one can evaluate the work of the external forces W. Since the material is linear elastic, each effort is proportional to the displacement of the application point. Assuming that the loading device does not store energy, from the Clapeyron's theorem the elastic energy has the following expression.

$$W^{el} = \sum_{p=1}^{N} \frac{1}{2}\, f_x^p\, u_x^p + \frac{1}{2}\, F_x^1\, U_x^{imp}$$

The application of Castigliano's theorem provides the following relation:

$$\frac{\partial W^{el}}{\partial U_i} = F_i \tag{9}$$

in which U_i and F_i denotes the displacement and force associated to the same dof. The application of this relation to the imposed displacement leads

$$\frac{\partial W^{el}}{\partial U_x^{imp}} = F_x^1 \tag{10}$$

which can be developed as:

$$\frac{\partial W^{el}}{\partial U_x^{imp}} = \sum_{p=1}^{N} \frac{1}{2}\, f_x^p\, \frac{\partial u_x^p}{\partial U_x^{imp}} + \frac{1}{2}\, F_x^1 \tag{11}$$

The expression for the term $\frac{\partial u_x^p}{\partial U_x^{imp}}$ is known from the specific kinematics imposed by the KUBC, i.e.,

$$\frac{\partial u_x^p}{\partial U_x^{imp}} = \frac{x^p}{L} \tag{12}$$

Finally, by combining eq (9), eq (11) and eq (12) the following relation is obtained:

$$\sum_{p=1}^{N} x^{(p)}\, f_x^{(p)} = F_x^{(1)}\, L \tag{13}$$

Each quantity involved in eq (7) is therefore measurable from the knowledge of global forces on each side. As an important consequence, in the situation of KUBC, the average stress $\underset{\sim}{\Sigma}$ can be computed in a realistic experimental setup. The final formula is given in eq (14).

$$\underset{\sim}{\Sigma} = \frac{1}{L\,H} \begin{pmatrix} F_x^{(2B)} + F_x^{(2C)} - F_x^{(3B)} + F_x^{(4C)} & -F_x^{(1D)} + F_x^{(2C)} + F_x^{(4C)} + F_x^{(4D)} \\ F_y^{(2B)} + F_y^{(2C)} - F_y^{(3B)} + F_y^{(4C)} & -F_y^{(1D)} + F_y^{(2C)} + F_y^{(4C)} + F_y^{(4D)} \end{pmatrix} \tag{14}$$

Where $F_y^{(2C)}$ is the effort over $\underline{y}$ on the edge ② applied at the point C. Points and edges are reminded on fig 6. Once again, the expression of $\underset{\sim}{\Sigma}$ is not symmetrical due to the choice of the origin on a corner of the domain. Actually, the expression of sigma given here is very dependant on the choice of the origin. However, when determining the experimental values, a symmetric expression is expected.

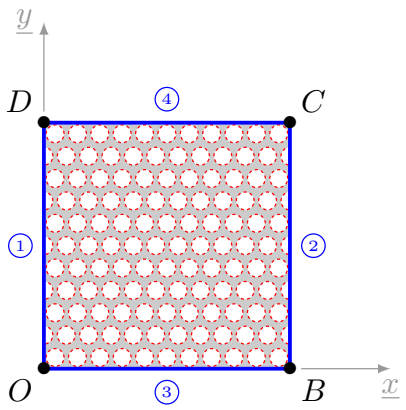

Figure 6: Reminder of notations Ω

To conclude this preliminary analysis of the necessary measurement technique, the reader must keep in mind that a global-type solution seems reasonable since global force are sufficient. The force required to deform the device must be negligible compared to that of the sample or at least of the same order of magnitude so as not to mask the latter. It is then necessary to be able to determine the force due to the device alone in order to decouple the two contributions measured by the global load cells, **which is the main goal of section 4**.

Last, it is also noteworthy that even if the device uses a 'global' force measurement for homogenization, one may use full-field measurement techniques to obtain the pantograph strain, and by use of its model, assess the forces transmitted at the specimen interface. The homogenization by KUBC being the main purpose of the device, the pantographs are designed to be stiff in comparison to the specimen, and this secondary load measurement technique might be not optimal, but this principle must be kept in might for future applications.

3. ... to an experimental context

3.1. Mechanism

Some devices using the idea of a linearly deformable frame have already been proposed, for research context as the $1\gamma 2\varepsilon$ device [20] (fig 7a) or in an industrial context by Accupull© (fig 7b) for example. The machine by Accupull© uses this idea as a way to distribute normal loading in a very large strain range in the context of plastic injection mold studies. Consequently

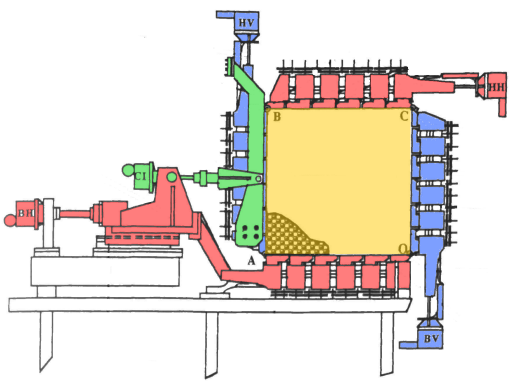

(a) $1\gamma 2\varepsilon$ device - [20]

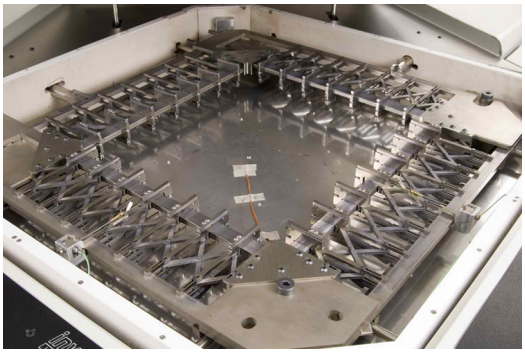

(b) Biaxal pulling machine by accupull©

Figure 7: Testing machines using pantographs to apply rich edge conditions

displacement accuracy at small strain scale is not of utmost importance and only bi-axial tension is considered. In [20] the frame is intended to apply also shear loads with a possibility to rotate the principal axes which corresponds to KUBC. However it was not conceive in the scope of homogenization and thus does not fulfil all the present requirements. The table 2 summarizes the specifications of these devices and the ones of the intended device.

Testing device	$1\gamma 2\varepsilon$-device	accupull©	wanted device
sample size	650×550 mm^2	58×58 to 106×106 mm^2	300×300 mm^2
max extension	0.2%	700%	2%
max compression	0.2%	0%	2%
max shear angle	20^o	0^o	2^o
load capa/fastener	100 kN	0.2 kN	0.2 kN
fasteners by side	5	7	10
max displ error	unknown	$> 5\,000$ µm	120 µm

Table 2: Comparison of existing and wanted testing device

In both examples the deformable frame consists of four pantographs assembled around the sample. An example of such a system is given in fig 8. This mechanism is constituted of rigid arms and pivots joints. The longitudinal strain of the structure is a soft mode: no strain energy is associated to it. All other modes involve the stiffness of the bars, so that imposing the kinematic of two joints amounts to impose the kinematic of the whole

structure. Consider for example the device depicted on fig 8. The peculiar kinematic of the assembly gives:

$$\begin{cases} \underline{\mathrm{u}}(0) = 0\,\underline{\mathrm{e}}_x \\ \underline{\mathrm{u}}(L) = a\,\underline{\mathrm{e}}_x \\ \underline{\mathrm{u}}(x) = \dfrac{a}{L}x\,\underline{\mathrm{e}}_x \end{cases}$$

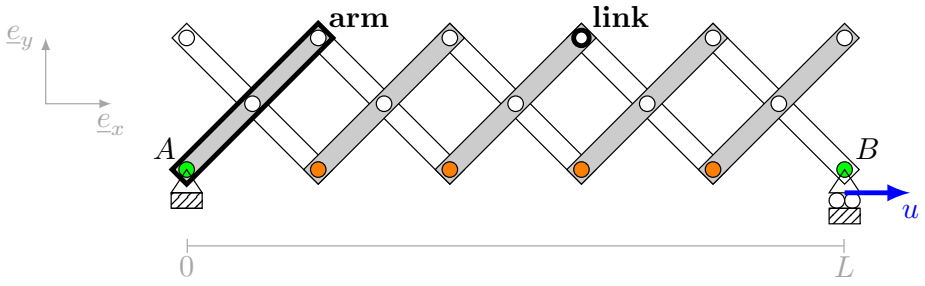

Figure 8: Schematic diagram of a pantograph

A pantographic based solution thus seems to be well-adapted to our needs [30] (fig 9) since it gives exactly a discrete kinematic uniform condition.

3.2. Technological choices

Now that the main idea of the mechanism has been defined the technological implementation has to be detailed. In order to minimize the errors in the imposed kinematics, clearances should be avoided as much as possible. Similarly, all sources of dissipation will be circumvent if possible. Dissipation sources and clearance will be called *indeterminate* later.

Two technological solutions for the design of the pantograph will be discussed below:

1. Bearing-based solution;
2. Flexible Link (FL)-based solution.

3.2.1. Ball-bearing based solution

A ball-bearing based solution minimises the energy losses but the clearance problem remains. For a centimetric bearing, the clearance with normal adjustment is around $c = 5$ µm, which gives for a pantographic structure:

- *Axial error:* A pantograph is composed of a series of assembled elementary cells. Each cell causes an elementary error that will proportionally

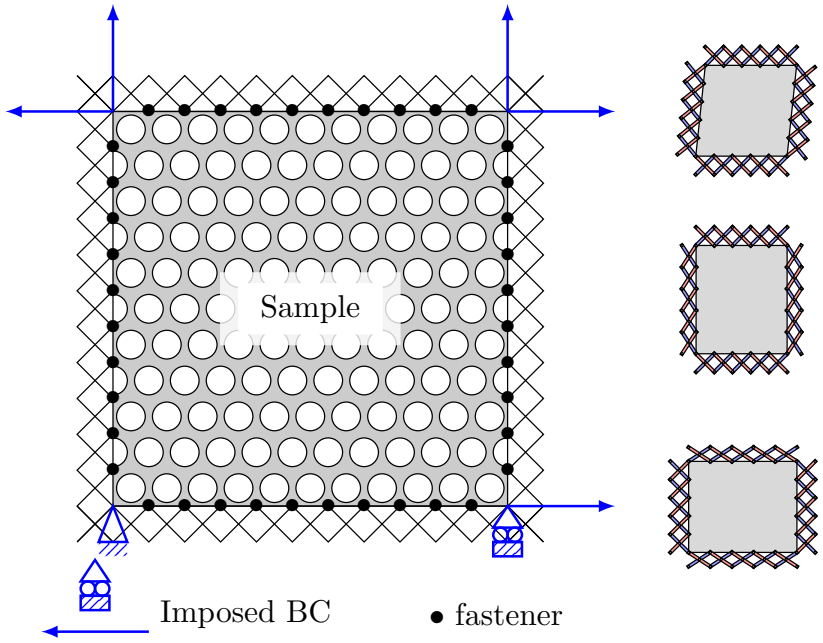

Figure 9: Field application device by pantographic frame and the three elementary applicable strain states

accumulate along the pantograph. This implies an error of $2nj$ for a n elementary cells pantograph making 100 µm here.

- *Transverse error:* Due to the bending of the pantograph, the spurious transverse displacement is much bigger than the axial one. A simple geometric construction gives $e_{bend} = n\sqrt{2}\left(1 + \frac{n(n-1)}{2}\right) j > 2.5$ mm with a small angle hypothesis. The transverse guiding error can be reduced to about 0 by constraining the pantograph displacement on rails. This solution is adopted by [20] and Accupull©.

Since the a total displacement should remains below 120 µm, this solution involving 100 µm error without taking into account the deformation of the component parts is not suitable. In addition, even if the dissipation of a bearings are very low, the large number of bearings and the very strong hyperstatism of the mechanism may generate significant energy losses. We will therefore consider another solution.
Given that the in-plane strain range is quite low, a solution based on flexible links is possible. The principle of a flexible link is to provide a pivot connection by elastic deformation of a thin part (fig 10). Such a connection has no

clearance and no energy dissipation as long as the link remains in its elastic domain. Stiffness and maximum rotation angle of the pivot depend on the mechanical properties of the material (Young modulus and elastic limit) and on the geometry of the thin part R, h and b (fig 10). However, these links are delicate: they can only withstand low rotation and low shear load. They have to be carefully sized.

3.2.2. Flexible link based solution

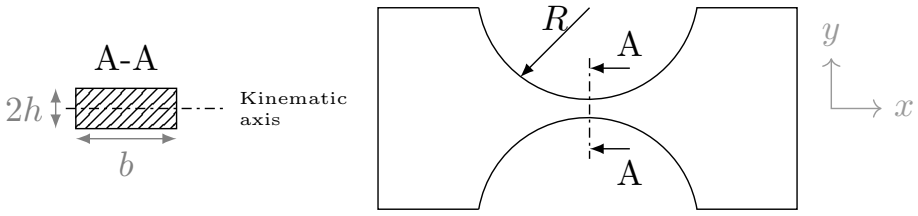

Figure 10: Description of a flexible link and its minimum section

First, have a look to the global mechanism under load to determine the static equilibrium and the forces in the links (fig 11). It should be noted that even if the mechanism seems to be a lattice, the beams have three pivot links and then do not work only in tension/compression.

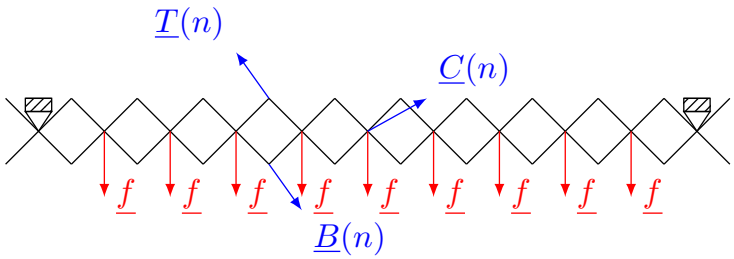

Figure 11: Loading of the pantograph

A static equilibrium of the pantograph gives the magnitude and the orientation of the efforts transiting through the Flexible Links (FL) (fig 12).

A significant misalignment of forces occurs at the ends of the pantograph (fig 12b). To overcome the problem of shear of the FL that this causes, three FL will be placed on each axis of rotation at 0, +30 and -30 degrees with respect to the pantograph axis (fig 13). The maximum loading of the links

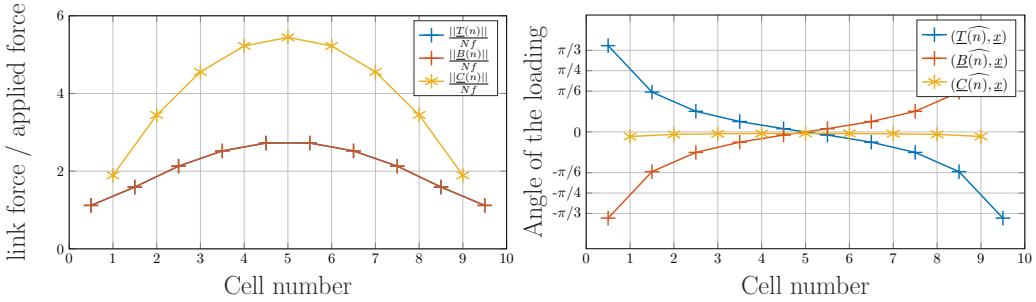

(a) Magnitude according to the total effort applied nf

(b) Orientation with respect to pantograph axis

Figure 12: Efforts transiting through the FL

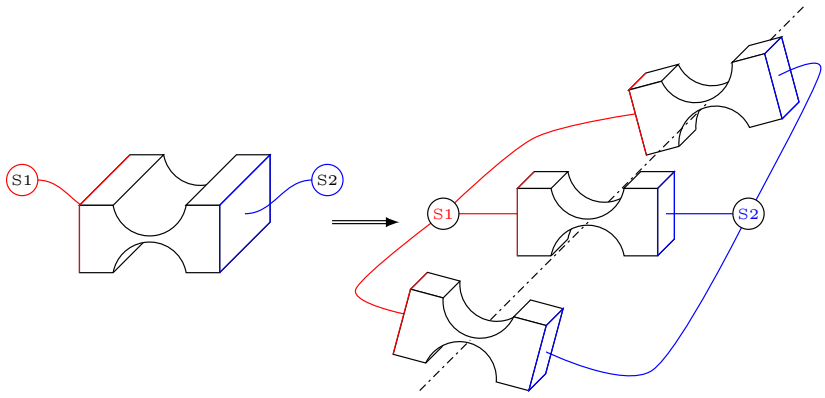

Figure 13: Decomposition of 1 FL to three parrallel tilted FL

gives their minimal section according to the yield strength of the material.

A variable section beam study [31] gives the maximum angle of rotation of flexible connections according to material and geometric parameters:

$$\omega_{max} = 2\,C\left(\frac{R}{h}\right)\,\frac{R}{h}\,\frac{R_e}{E}$$

with $C\left(\frac{R}{h}\right)$ a monotonic function only dependent on $\dfrac{R}{h}$.

A Modulus - Strength chart from [4] gives elastomers and polymers as best results for the flexible links according to this criterion. However all the pantograph will be made in this material and the arms must be rigid enough

to impose their kinematic to the sample. **Moreover they are materials with hysteric mechanical behavior, which one must avoid to ensure a bijection between force and displacement. For these reasons** they will not be retained. The next choices are titanium alloys, magnesium alloys and aluminium alloys. For cost reasons we will choose 7000 series aluminium alloys for constitutive material.

Thus, taking into account the desired space requirement, the following set of parameters is obtained for a 7075 aluminium alloy

$$\begin{cases} R_e \simeq 430 \text{ MPa} \\ E = 72 \text{ GPa} h = 0.7 \text{ mm} \\ b = 100 \text{ mm} \\ R = 3 \text{ mm} \end{cases}$$

This configuration with a simple pantograph does not seem viable. Actually, to machine a thin part of 0.7 mm through a 100 mm aluminium sheet is not conceivable. Thereby a multi rows pantograph is considered as shown on fig 14. The desired device (fig 15d) will then be constituted of two stages (fig 15c), each composed of three layers (fig 15b) of four pantographs (fig 15a) with multiple rows.

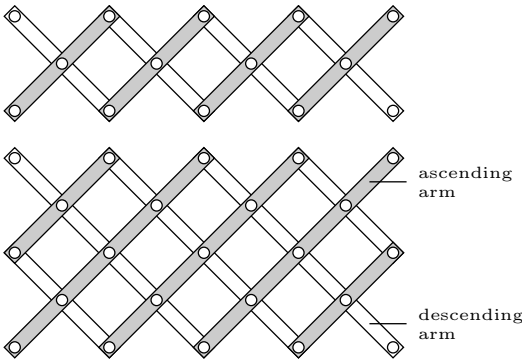

Figure 14: 1 and 2 rows pantograph

The sample will take place between the two stages (fig 15d) to ensure an in-plane loading. The three layers are the result of the choice of three orientations of flexible links. In such a situation the static equilibrium can not be written easily and a numerical resolution is mandatory.

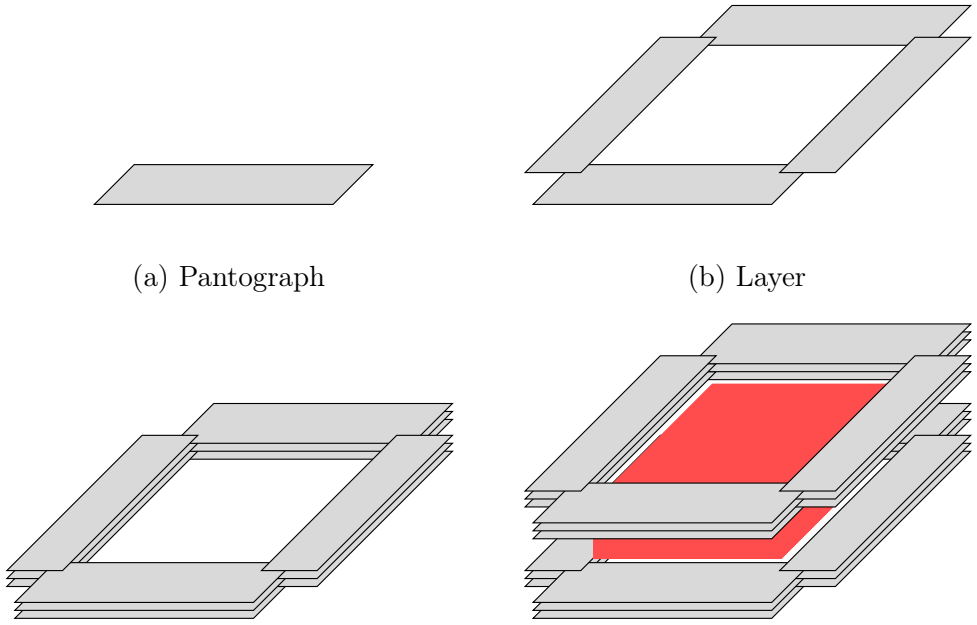

(a) Pantograph (b) Layer

(c) Stage (d) Device (sample in red)

Figure 15: Composition of the device

3.3. Overall geometry

The geometries of the arms are obtained by maximizing their global rigidity while maintaining the functional surfaces necessary for operation (fig 16).

It is worth noting that the relation between the kinematic of the arms and their geometry is not straightforward, the pivot connections seeming located at the screw bores while they are in fact at the FL neck. The kinematics of the assembly is shown on fig 17.

Now that the main shapes of the arms have been determined, the geometrical parameters have to be optimized. However a global computation is not conceivable because of the very thin parts that tremendously increase the cost of calculation. To avoid mesh dependency, at least 500 000 dof per arm are necessary, leading to more than 3×10^8 dof in the case of fig 15d. The associate numerical cost is prohibitive and justifies the creation of a specific numerical tool.

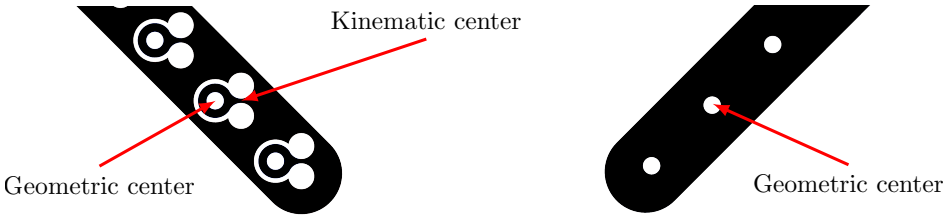

(a) Flexible arm (b) Rigid arm

Figure 16: Shape of the arms

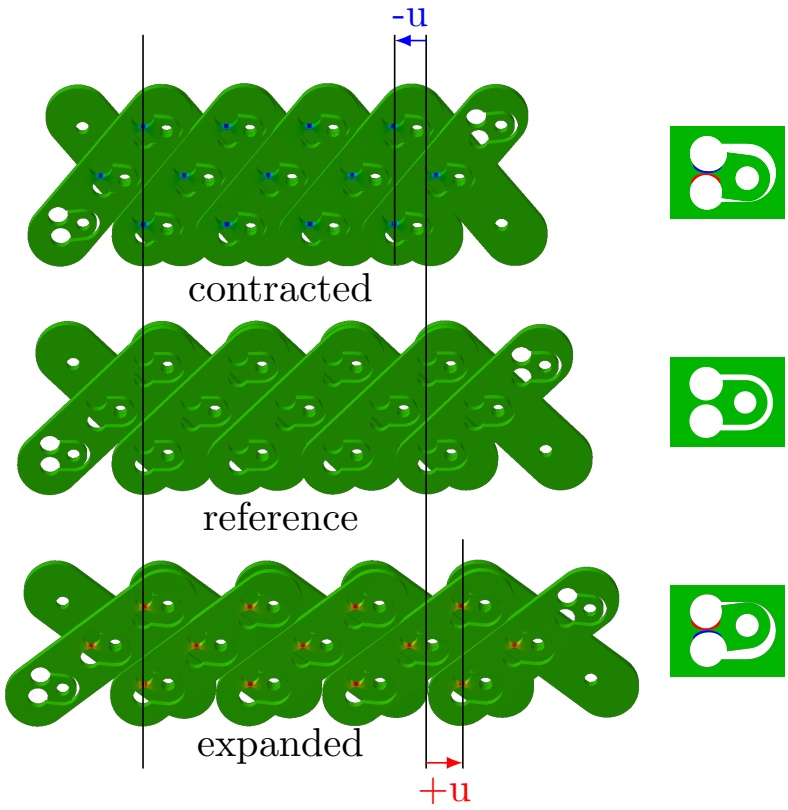

Figure 17: kinematics of the pantograph with flexible links and correlated deformations of the FL

4. Creation and validation of the VTD

A multiple rows pantograph can be seen as a lattice with specific macro-elements: each element represents an arm with multiple anchors. Thus, to simulate the behaviour of the pantograph, it is sufficient to determine the

behaviour of the arms and then to make a lattice with the adequate elements. Two types of arms will be considered: flexible and rigid, the flexible links being included in the flexible arms. Each node of the macro-elements possesses all the in-plane dof: two translations u_x, u_y and one rotation ω_z.

As can be seen in fig 15d the complete device is composed of 2 stages of 4 pantographs with 3 layers of multiple arms. This composition will guide the main steps in the development of the numerical code.

1. Stiffness matrices of the arms $[k]$ are determined by Finite Element (FE) simulation.
2. Matrices of single-layer pantographs $[K]$ are build with the elementary ones.
3. Three-layer pantographs matrices $[\mathcal{K}]$ are obtained by tying the $[K]$ matrices together by [K].
4. Global stiffness matrix of the device $[\mathbb{K}]$ is constructed by binding the $[\mathcal{K}]$ matrices by their corners with $[\kappa]$.

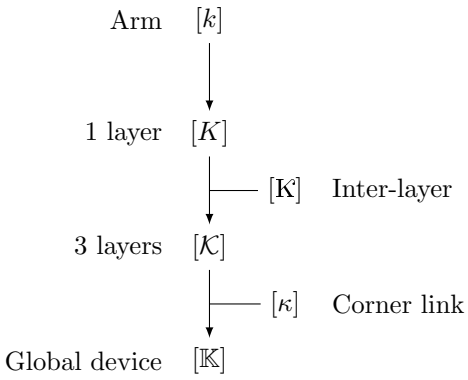

The same symbolism will be used for displacements and forces (table 3).

The reader must pay attention to the notion of subscript. Here, subscripts refer to the nodes and therefore to 3 dof, consequently $[\,\cdot_{(ij)}]$ is not a scalar but a 3x3 matrix.

4.1. Elementary matrix calculation

Since it is necessary to control the pantograph by the axes of the pivots to impose the sought kinematics, it is simpler to express the elementary stiffness matrix $[k]$ at the center of the flexible links (kinematic centres) rather than at their ends (geometric centres) (fig 16).

'scale'	stiffness matrix	displacement	force	subscript
arm	$[k]$	$[u]$	$[f]$	i, j
1 layer	$[K]$	$[U]$	$[F]$	I, J
3 layers	$[\mathcal{K}]$	$[\mathcal{U}]$	$[\mathcal{F}]$	α, β
global device	$[\mathbb{K}]$	$[\mathbb{U}]$	$[\mathbb{F}]$	Γ, Δ

Table 3: Symbolism used in the description of the construction of the global stiffness matrix

To do so, ones modifies the geometry so that the mechanical assemblies are the same as the kinematic assemblies, leading to the design depicted on fig 18. The number of flexible links N_F on each arm depends on the number of rows of the pantograph.

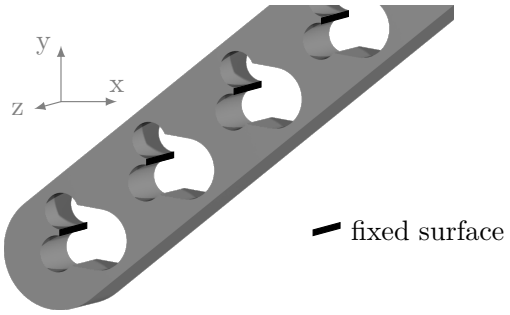

Figure 18: FE simulation for elementary matrix determination

The elementary stiffness matrices are computed row by row by computing the reaction associated to each elementary dof:

$$[f] = \left[[f_{x_1}, f_{y_1}, m_{z_1}], \ldots, [f_{x_j}, f_{y_j}, m_{z_j}], \ldots, \left[f_{x_{N_F}}, f_{y_{N_F}}, m_{z_{N_F}} \right] \right]$$

and the results are concatenated:

$$
[k] = \begin{array}{c} \\ u_{x_1} \\ u_{y_1} \\ \omega_{z_1} \\ \vdots \\ u_{x_i} \\ u_{y_i} \\ \omega_{z_i} \\ \vdots \\ u_{x_{N_F}} \\ u_{y_{N_F}} \\ \omega_{z_{N_F}} \end{array}
\begin{array}{c}
\begin{array}{ccccccc} f_{x_1} & \dots & f_{x_j} & f_{y_j} & m_{z_j} & \dots & m_{z_{N_F}} \end{array} \\
\left[\begin{array}{ccccccc}
 & & & & & & \\
 & & & & & & \\
 & & & & & & \\
 & & & \left[\quad [k_{(ij)}] \quad\right] & & & \\
 & & & & & & \\
 & & & & & & \\
 & & & & & &
\end{array}\right]
\end{array}
$$

with $[k_{(ij)}]$ the (3×3) stiffness matrix related to the nodes i and j of the same arm. Since the complete device is made of two types of arms (R,F), having 3 specific orientations (U,M,D) the elementary matrices are of 6 different type.

$$
\begin{bmatrix} k^{FU} \end{bmatrix} \quad \begin{bmatrix} k^{FM} \end{bmatrix} \quad \begin{bmatrix} k^{FD} \end{bmatrix} \quad \begin{bmatrix} k^{RU} \end{bmatrix} \quad \begin{bmatrix} k^{RM} \end{bmatrix} \quad \begin{bmatrix} k^{RD} \end{bmatrix}
$$

where the top letters are used to describe the arm geometry:

$$
\begin{cases} F & : \text{ Flexible arm} \\ R & : \text{ Rigid arm} \end{cases} \qquad \& \qquad \begin{cases} U & : \text{ Upwards link (30 deg.)} \\ M & : \text{ Mid link (0 deg.)} \\ D & : \text{ Downwards link (-30 deg.)} \end{cases}
$$

4.2. Building of a layer

The local matrices have to be assembled two by two to obtain the stiffness of a pantograph. Since the flexible and rigid arms that have the same orientation create a layer, three layers are obtained:

$$
\begin{bmatrix} K^X \end{bmatrix} \quad \text{With } X = \{U, M, D\}
$$

Each layer's stiffness matrix expresses as follow and is illustrated on fig 19.

$$
\begin{bmatrix} K^X_{(IJ)} \end{bmatrix} = \chi_R(I,J) \quad \begin{bmatrix} k^{RX}_{(ij)} \end{bmatrix} + \chi_F(I,J) \quad \begin{bmatrix} k^{FX}_{(ij)} \end{bmatrix}
$$

Where

I and J are the indices of the nodes in the layer
i and j are the corresponding indices in the arm

with

$$\begin{cases} \chi_R(I,J) = 1, & \text{if } I \text{ and } J \text{ are nodes of the same rigid arm} \\ \chi_R(I,J) = 0, & \text{otherwise} \end{cases}$$

$$\begin{cases} \chi_F(I,J) = 1, & \text{if } I \text{ and } J \text{ are nodes of the same flexible arm} \\ \chi_F(I,J) = 0, & \text{otherwise} \end{cases}$$

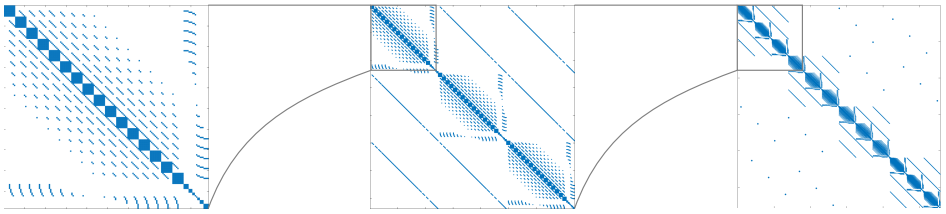

Stiffness matrix of a layer : $[K]$

Stiffness matrix of a 3-layer pantograph : $[\mathcal{K}]$

Stiffness matrix of an assembly of 4 pantographs : $[\mathbb{K}]$

Figure 19: Filling of the stiffness matrices

4.3. Tying the layers

Having assembled all the elements has lead to four series (sides) of three layers of pantographs. It is then necessary to connect the three layers of the same side. One can not simply impose an identical kinematics on the stacked nodes, because the centres of the flexible links of the three layers do not strictly have the same displacement. The points with the same displacement from one layer to another are the centers of the holes (geometric centres on fig 16a and fig 16b). However these points do not belong to the lattice, so we can not impose conditions on.

To overcome this problem, an other macro-element, of stiffness matrix $[\mathfrak{k}]$, corresponding to the rigidity between the layers is introduced. This makes it possible to make the link between the nodes of the different layers. The detail of its determination is given in Appendix B

The stiffness matrix between three superposed nodes of three layers $[\mathfrak{k}]$ can be split in $[\mathfrak{k}_{ab}]$ depicting the stiffness between the nodes of the layer a and b.

$$[\mathfrak{k}] = \begin{bmatrix} \left[\mathfrak{k}_{(UU)}\right] & \left[\mathfrak{k}_{(UM)}\right] & \left[\mathfrak{k}_{(UD)}\right] \\ \left[\mathfrak{k}_{(MU)}\right] & \left[\mathfrak{k}_{(MM)}\right] & \left[\mathfrak{k}_{(MD)}\right] \\ \left[\mathfrak{k}_{(DU)}\right] & \left[\mathfrak{k}_{(DM)}\right] & \left[\mathfrak{k}_{(DD)}\right] \end{bmatrix}$$

This allows to link the layers and build the stiffness matrix of the three-layer pantographs $[\mathcal{K}]$:

$$[\mathcal{K}] = \begin{bmatrix} [K] & & \\ & [K] & \\ & & [K] \end{bmatrix} + [\mathbb{K}]$$

with

$$\left[\mathbb{K}_{(\alpha\beta)}\right] = \sum_{a=\{U,M,D\}} \sum_{b=\{U,M,D\}} \delta^l_{\alpha a}\, \delta^l_{\beta b}\, \delta^c_{\alpha\beta}\ \left[\mathfrak{k}_{(ab)}\right]$$

where

$$\begin{cases} \delta^l_{\alpha a} = 1 & \text{if } \alpha \in \text{layer } a \\ \delta^l_{\alpha a} = 0 & \text{otherwise} \\ \\ \delta^c_{\alpha\beta} = 1 & \text{if } \alpha \text{ and } \beta \text{ have the same coordinates} \\ \delta^c_{\alpha\beta} = 0 & \text{otherwise} \end{cases}$$

δ^l being a Kronecker like symbol that defines the belonging to a layer and δ^c a Kronecker like symbol for the coordinates of the nodes.

4.4. Imposing BC

Finally, it remains to connect the 4 sides. It is desired that the translations be transmitted between the sides but that the rotations are not in order to impose shear on the specimen. The rotations of the sides must therefore be independent. To impose it numerically, a method by penalization is applied:

$$[\mathbb{K}] = \begin{bmatrix} [\mathcal{K}] & & & \\ & [\mathcal{K}] & & \\ & & [\mathcal{K}] & \\ & & & [\mathcal{K}] \end{bmatrix} + [\kappa]$$

with

$$[\kappa] = \chi_{pena}(\Gamma, \Delta)\, \mathbf{k}$$

where

$$\begin{cases} \chi_{pena}(\Gamma,\Delta) = 1, & \text{if } \begin{cases} \Gamma = \Delta \\ \Gamma \in LPD \end{cases} \\ \chi_{pena}(\Gamma,\Delta) = -1, & \text{if } \begin{cases} \Gamma \neq \Delta \\ (\Gamma,\Delta) \in LPD \end{cases} \\ \chi_{pena}(\Gamma,\Delta) = 0, & \text{otherwise} \end{cases}$$

LPD is the List of Penalized couples of Degrees of freedom. This amounts to hook a spring of stiffness $\mathbf{k}$ between the dofs.

$$\mathbf{k} = 10^{p+q/2}$$

with

$$\begin{cases} p & \text{order of magnitude of the larger term of the matrix} \\ q & \text{number of significant digits with which the software works} \end{cases}$$

The value of $\mathbf{k}$ is determined so as not to deteriorate the conditioning of the overall stiffness matrix while ensuring a good bond of the dofs [13]. Unlike a substitution method or a Lagrange multipliers method, the penalization method is not exact. However, it is much simpler to implement and generates smaller errors than those due to the numerical determination of the local stiffness matrices.

It is thus possible to simulate the behaviour of a complex set of pantographs and to deduce the displacements of each of the nodes (kinematic centers).

To achieve the sizing of the arms it is necessary to know the displacement of the nodes (to minimise the maximum error of the device) but also to ensure its mechanical resistance. To do so, the mechanical actions transiting through each FL are calculated by using the kinematical results and the elementary stiffness matrices of the arms $[k]$.

$$[f] = [k]\ [u]$$

Where $[u]$ and $[f]$ are respectively the displacement and mechanical actions on the nodes of a macro-element and so on the FL of an arm.

$$[f] = \left[[f_{x_1}, f_{y_1}, m_{z_1}], \ldots, \left[f_{x_j}, f_{y_j}, m_{z_j}\right], \ldots, \left[f_{x_{N_F}}, f_{y_{N_F}}, m_{z_{N_F}}\right] \right]$$

The stress state in each FL can then be obtained thanks to the knowledge

of the mechanical actions transiting through it $[f_{x_i}, f_{y_i}, m_{z_i}]$ by superposition of previously calculated elementary stress states: 3 FE calculations are conducted on a FL, on each the link is subjected to an elementary loading corresponding to a degree of freedom of the plane.

$$[f_{x_i}, f_{y_i}, m_{z_i}] = [1,\ 0,\ 0] \Rightarrow \underset{\sim x}{\hat{\sigma}^0}$$
$$[f_{x_i}, f_{y_i}, m_{z_i}] = [0,\ 1,\ 0] \Rightarrow \underset{\sim y}{\hat{\sigma}^0}$$
$$[f_{x_i}, f_{y_i}, m_{z_i}] = [0,\ 0,\ 1] \Rightarrow \underset{\sim z}{\hat{\sigma}^0}$$

where $\underset{\sim X}{\hat{\sigma}^0}$ (with $X = \{x, y, z\}$) are the elementary stress state used to determine real stress state:

$$\underset{\sim i}{\sigma} = \sum_{X=\{x,y,z\}} f_{X_i}\ \underset{\sim X}{\hat{\sigma}^0}$$

where $\underset{\sim i}{\sigma}$ is the stress state of the i-th link of the arm. Knowing the stress state in the link, an equivalent Von Mises stress can be computed to ensure that the links remain in their elasticity domain.

4.5. Validation

To control the validity of the proposed numerical model, full-field simulations of the device are conducted. In order to be as close as possible to the real device, the simulation presented in fig 20 is considered. A three layer pantograph with one row and 5 fasteners is studied. However the number of nodes, layers, ... are lower than on the complete device, all the technical difficulties are represented:

- special arms are used to impose the kinematic of the pantograph (arms with green cylinders);
- important out-of-plane dimension because of the 3 layers and the anchors while the reduced model is in-plane;
- complementary parts, called anchors, are fixed on the arms of the pantograph (through the orange faces on fig 20) to make the link with the specimen. The static conditions are imposed on the anchors, on the blue areas (fig 20).

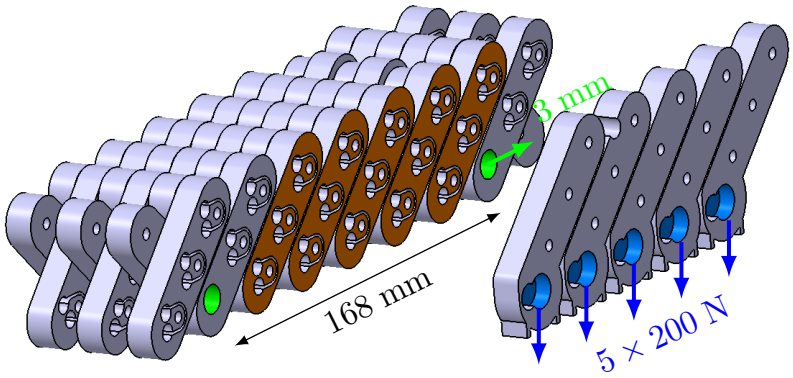

Figure 20: Assembly used for the validation of the first step.
- green cylinders : imposed kinematics
- orange faces : fixed to the anchors
- blue area : imposed statics

Specific macro-elements obtained by FE-simulations are used to describe these new parts. The pantograph is subjected to maximum solicitations: 2% extension and 200 N per anchor.

This simulation represent a numerical cost of 8.10^6 dofs with T6 elements for a converged solution. The equivalent reduced model, presented in fig 21 represents a numerical cost of less than 1.10^2 dofs, with 13 preliminary calculations of the elementary matrices (13 different arms including the special ones used to impose the kinematic and the static conditions), with around 1.10^5 dofs each. For such a computation the benefit of the reduced model is not very important, however for the complete device the number of nodes associated to the reduced model does not increase significantly while the one associated to the full-field simulation is multiplied by more than 30 (table 4).

	preliminary calculations	global simulation
full-field	0	3.10^8 dfos
reduced model	13×2.10^5 dofs	4.10^3 dofs

Table 4: Calculations costs associated to the complete device

The figure 22 presents the displacement disparities in µm between the full-field computation (reference) and the reduced model for the nodes (centres of FL) on which the sample will be tied. A maximum of 8 µm of difference are observed, that represent 0.3% of the solicitation (3 mm).

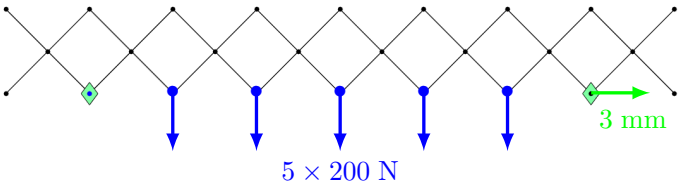

Figure 21: Reduced model.
- green diamond : imposed kinematics
- blue dots : imposed forces.

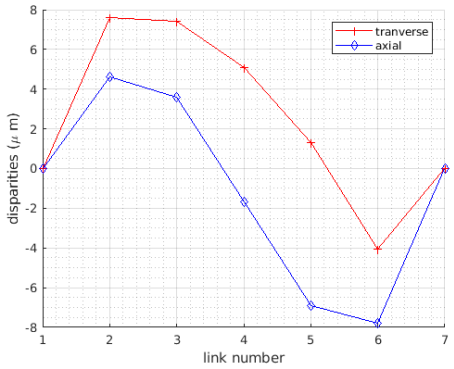

Figure 22: Displacement disparities between full-field computation and reduced model

Finally, the model gives the possibility to simulate a multi rows and multi layers pantograph with kinematic and static discretized conditions and return the displacements and an evaluated maximum Von Mises criterium on the flexible links.

4.6. Sizing

The specifications given in table 2 are considered : a maximum of 120 µm of error on the imposed kinematic is allowed, representing 2% of the solicitation range under maximal static loading. Computations on the reduced model are conducted to obtain the optimized geometrical parameters (fig 23).

The thickness and radius of the flexible links are chosen in order to stay in the elastic domain and to ensure the solicitation range (6 mm).

The thickness of the arms, the number of rows and the global geometry of the arms are chosen in order to ensure kinematic precision and realistic machining process.

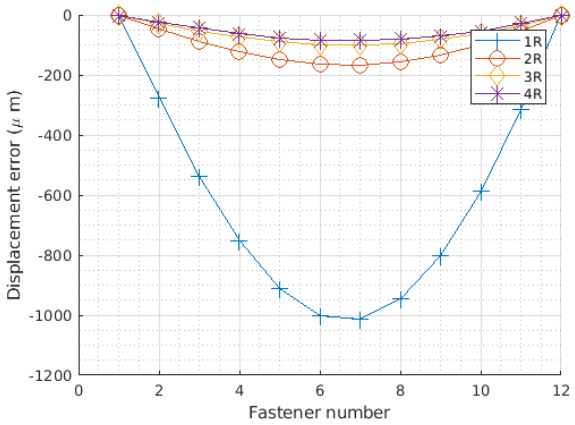

Figure 23: Evolution of bending error (μm) with the numbers of rows for the maximum loading (200 N/fastener)

The following set of parameters is obtained in the case of a 7075 aluminium alloy:

$$\begin{cases} 2h = 0.7 \text{ mm} \\ b = 10 \text{ mm} \\ R = 3 \text{ mm} \\ N_R = 3 \end{cases}$$

in which N_R the number of rows. Compared to the previous set, the thickness of the arms has been divided by 10 by multiplying the number of rows by 3 while keeping the same kinematic precision. A Computer Aided Design (CAD) overview of the complete device is given in fig 24 on which a sample is shown.

The table table 5 gives the main characteristics of the device, specific terms are defined on fig 15 and fig 10.

5. Conclusion and perspectives

An adaptation of mean field homogenization by KUBC to an experimental framework has been exposed. This adaptation is possible thanks to, two major points:

- a method for determining the average stress field over the specimen by realistic measuring means (global measurements on the edges of the specimen);

Global specifications	
- material	7075 aluminium alloy
- sample size	$300 \times 300 \times 20$ mm^3
- control point / side (2dof)	10
- assembly size	$500 \times 500 \times 400$ mm^3
- stages	2
- layers	3
- rows	3
- flexible links	2376
- $2h$	0.7 mm
- R	3 mm
- b	10 mm

Table 5: General characteristics of the device

- an innovative design of an experimental device allowing the application of discretized Kinematic Uniform Boundary Conditions on the edges of a 300 mm square specimen. The use of pantographs for the repartition of the displacement on the edge allows the use of a small number of actuators (5) to control the displacement of all the points on the boundary. The realization of the pantographs by flexible links permits to eliminate all the clearance and the major part of non-linear dissipations of the pantograph.

A reduced model of the device has been proposed by assimilating the arms of the pantograph to macro-elements. This reduced model has been used to size the device and will later be used:

- before the tests to predict and adapt test conditions;
- after the test, by using this model in an inverse approach it will be possible to determine the loading repartition on the boundary of the specimen by measuring the displacement of the device (Digital Image Correlation).

Subsequently, the manufacture of the machine and the validation of its characteristics will have to be finalized before carrying out homogenization tests. These tests will be coupled with a numerical study in order to highlight

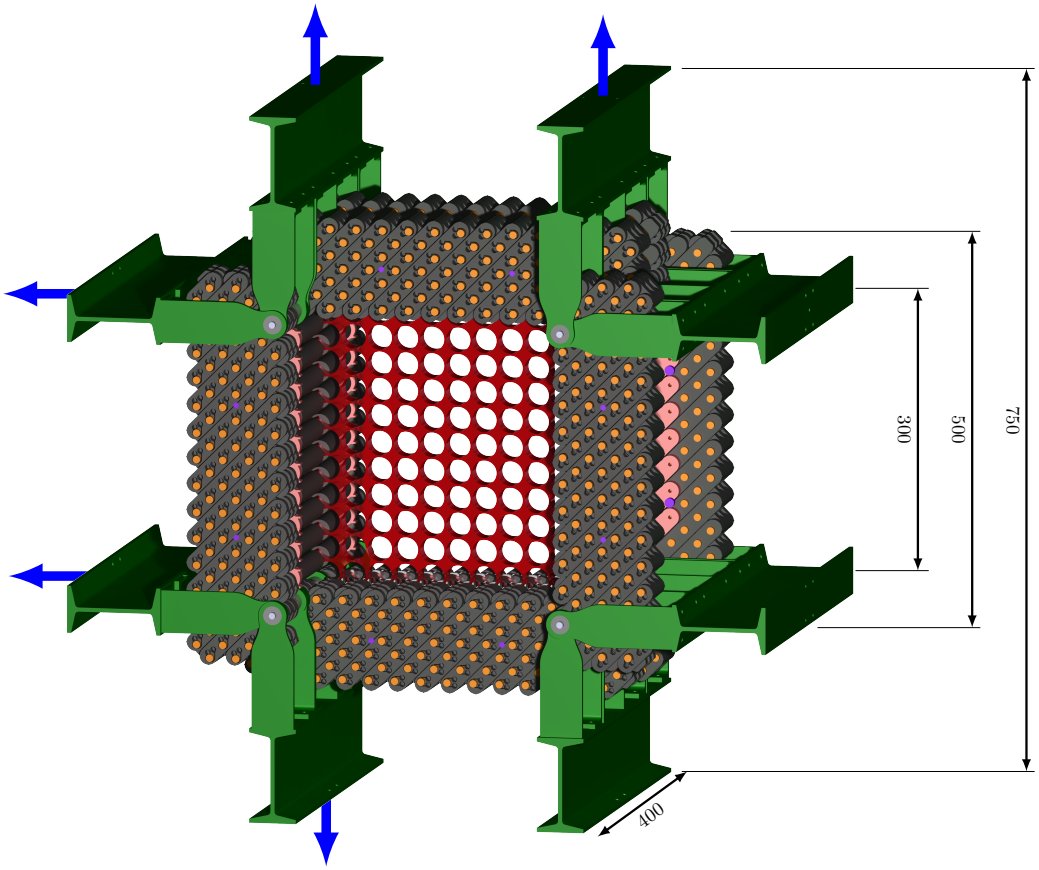

Figure 24: CAD overview of the design and a specimen (in red)
$\rightarrow$ to actuator

the disparities observed on the apparent behaviour due to defects of the material. A sensitivity study to the imperfection of the boundary conditions should also be carried out.

References

[1] Abdoul Anziz, H. (2018). *Homogénéisation de composites élastiques périodiques à fort contraste : Conception de métamatériaux de second gradient.* thesis, Toulon.

[2] Abdoul-Anziz, H. and Seppecher, P. (2017). Strain gradient and generalized continua obtained by homogenizing frame lattices.

[3] Allaire, G. and Schoenauer, M. (2007). Optimisation topologique par

méthoded'homogénéisation. In *Conception optimale de structures*, volume 58, pages 163–175. Springer.

[4] Ashby, M. F. (2005). Material property charts. In *Materials selection in mechanical design*, pages 45–78. Butterworth-Heinemann, Amsterdam ; Boston, 3rd ed edition.

[5] Ashby, M. F. and Bréchet, Y. J. M. (2003). Designing hybrid materials. *Acta Materialia*, 51(19):5801–5821.

[6] Barclift, M. and Williams, C. (2012). Examining variability in the mechanical properties of parts manufactured via polyjet direct 3d printing. *23rd Annual International Solid Freeform Fabrication Symposium - An Additive Manufacturing Conference, SFF 2012*.

[7] Barthelat, F. (2015). Architectured materials in engineering and biology: fabrication, structure, mechanics and performance. *International Materials Reviews*, 60(8):413–430.

[8] Bornert, M., Bretheau, T., and Gilormini, P. (2001). *Homogénéisation en mécanique des matériaux, Tome 1 : Matériaux aléatoires élastiques et milieux périodiques*. Hermes science.

[9] Bouaziz, O., Bréchet, Y., and Embury, J. D. (2008). Heterogeneous and Architectured Materials: A Possible Strategy for Design of Structural Materials. *Advanced Engineering Materials*, 10(1-2):24–36.

[10] Brechet, Y. and Embury, J. D. (2013). Architectured materials: Expanding materials space. *Scripta Materialia*, 68(1):1–3.

[11] Donders, P. G. (2018). *Homogenization method for topology optmization of struc-tures built with lattice materials.* PhD thesis, Université Pais-Saclay.

[12] Eberhardsteiner, J. (1995). Biaxial testing of orthotropic materials using electronic speckle pattern interferometry. *Measurement*, 16(3):139–148.

[13] Felippa, C. A. (2004). Introduction to finite element methods. *Course Notes, Department of Aerospace Engineeing Sciences, University of Colorado at Boulder, available at http://www. colorado. edu/engineering/Aerospace/CAS/courses. d/IFEM. d.*

[14] Feyel, F. (1999). Multiscale FE2 elastoviscoplastic analysis of composite structures. *Computational Materials Science*, 16(1-4):344–354.

[15] Fleck N. A., Deshpande V. S., and Ashby M. F. (2010). Micro-architectured materials: past, present and future. *Proceedings of the Royal Society A: Mathematical, Physical and Engineering Sciences*, 466(2121):2495–2516.

[16] Geers, M. G. D., Kouznetsova, V. G., and Brekelmans, W. A. M. (2010). Multi-scale computational homogenization: Trends and challenges. *Journal of Computational and Applied Mathematics*, 234(7):2175–2182.

[17] Hazanov, S. and Huet, C. (1994). Order relationships for boundary conditions effect in heterogeneous bodies smaller than the representative volume. *Journal of the Mechanics and Physics of Solids*, 42(12):1995–2011.

[18] Hill, R. (1963). Elastic properties of reinforced solids: Some theoretical principles. *Journal of the Mechanics and Physics of Solids*, 11(5):357–372.

[19] Huet, C. (1990). Application of variational concepts to size effects in elastic heterogeneous bodies. *Journal of the Mechanics and Physics of Solids*, 38(6):813–841.

[20] Joer, H. A. (1991). *" 1 [gamma] 2 [epsilon]": une nouvelle machine de cisaillement pour l'étude du comportement des milieux granulaires*. PhD Thesis, Université Joseph Fourier.

[21] Juneja, M., Thakur, N., Kumar, D., Gupta, A., Bajwa, B., and Jindal, P. (2018). Accuracy in dental surgical guide fabrication using different 3-D printing techniques. *Additive Manufacturing*, 22:243–255.

[22] Kanit, T., Forest, S., Galliet, I., Mounoury, V., and Jeulin, D. (2003). Determination of the size of the representative volume element for random composites: statistical and numerical approach. *International Journal of Solids and Structures*, 40(13):3647–3679.

[23] Li, N., Huang, S., Zhang, G., Qin, R., Liu, W., Xiong, H., Shi, G., and Blackburn, J. (2019). Progress in additive manufacturing on new materials: A review. *Journal of Materials Science & Technology*, 35(2):242–269.

[24] Moulinec, H. and Suquet, P. (1998). A numerical method for computing the overall response of nonlinear composites with complex microstructure. *Computer Methods in Applied Mechanics and Engineering*, 157(1):69–94.

[25] Parry, L., Ashcroft, I. A., and Wildman, R. D. (2016). Understanding the effect of laser scan strategy on residual stress in selective laser melting through thermo-mechanical simulation. *Additive Manufacturing*, 12:1–15.

[26] Poncelet, M., Somera, A., Morel, C., Jailin, C., and Auffray, N. (2018). An experimental evidence of the failure of Cauchy elasticity for the overall modeling of a non-centro-symmetric lattice under static loading. *International Journal of Solids and Structures*.

[27] Ranaivomiarana, N., Irisarri, F.-X., Bettebghor, D., and Desmorat, B. (2019). Concurrent optimization of material spatial distribution and material anisotropy repartition for two-dimensional structures. *Continuum Mechanics and Thermodynamics*, 31(1):133–146.

[28] Rosi, G., Placidi, L., and Auffray, N. (2018). On the validity range of strain-gradient elasticity: A mixed static-dynamic identification procedure. *European Journal of Mechanics - A/Solids*, 69:179–191.

[29] Sab, K. (1992). On the Homogenization and the Simulation of Random Materials. *Eur. J. Mech, . A/Solids*, pages 585–607.

[30] Seppecher, P., Alibert, J.-J., and Isola, F. D. (2011). Linear elastic trusses leading to continua with exotic mechanical interactions. *Journal of Physics: Conference Series*, 319(1):012018.

[31] S.Konieczka (1993). De la rigidité d'une liaison élastique calculée par la théorie des poutres.

[32] Summer, G. and Clayton, A. (1988). Structural Testing in Nuclear Engineering. *Butterworths, Full-Scale Fatigue Testing of Components and Structures*, 1(10):186–209.

[33] Tan, W. S., Suwarno, S. R., An, J., Chua, C. K., Fane, A. G., and Chong, T. H. (2017). Comparison of solid, liquid and powder forms of 3d printing techniques in membrane spacer fabrication. *Journal of Membrane Science*, 537:283–296.

[34] Tartar, L. (1989). Nonlocal Effects Induced by Homogenization. In Colombini, F., Marino, A., Modica, L., and Spagnolo, S., editors, *Partial Differential Equations and the Calculus of Variations: Essays in Honor of Ennio De Giorgi Volume 2*, Progress in Nonlinear Differential Equations and Their Applications, pages 925–938. Birkhäuser Boston, Boston, MA.

[35] Tymrak, B. M., Kreiger, M., and Pearce, J. M. (2014). Mechanical properties of components fabricated with open-source 3-D printers under realistic environmental conditions. *Materials & Design*, 58:242–246.

[36] Williams, R. J., Piglione, A., Rønneberg, T., Jones, C., Pham, M.-S., Davies, C. M., and Hooper, P. A. (2019). In situ thermography for laser powder bed fusion: Effects of layer temperature on porosity, microstructure and mechanical properties. *Additive Manufacturing*, 30:100880.

Appendix A. Detailed calculation of the mean stress

Starting from eq (5) :

$$V \underset{\sim}{\Sigma} = \sum_{p=1}^{4\,N} \int_{\partial\Omega^{(p)}} \left(\underset{\sim}{\sigma}^{(p)} \cdot \underline{\mathrm{n}}^{(p)} \right) \otimes \underline{\mathrm{x}} \ \mathrm{d}S$$

and using the linear decomposition of the stress

$$\underset{\sim}{\sigma}^{(p)}(\underline{\mathrm{x}}) \simeq \underset{\sim}{\sigma}^{0(p)} + \left(\underline{\mathrm{y}}^{(p)}(\underline{\mathrm{x}}) \cdot \underline{\mathrm{e}}^{(p)} \right) \ \underset{\sim}{\sigma}^{1(p)}$$

and the position

$$\underline{\mathrm{y}}^{(p)} = \underline{\mathrm{x}} - \underline{\mathrm{x}}^{(p)}$$

we have

$$\begin{aligned}
V \underset{\sim}{\Sigma} &= \sum_{p=1}^{4\,N} \int_{\partial\Omega^{(p)}} \left[\left(\underset{\sim}{\sigma}^{0(p)} + \underset{\sim}{\sigma}^{1(p)} \ \left(\underline{\mathrm{y}}^{(p)} \cdot \underline{\mathrm{e}}^{(p)} \right) \right) \cdot \underline{\mathrm{n}}^{(p)} \right] \otimes \left(\underline{\mathrm{x}}^{(p)} + \underline{\mathrm{y}}^{(p)} \right) \ \mathrm{d}S \\
&= \sum_{p=1}^{4\,N} \int_{\partial\Omega^{(p)}} \left(\underset{\sim}{\sigma}^{0(p)} \cdot \underline{\mathrm{n}}^{(p)} \right) \otimes \underline{\mathrm{x}}^{(p)} \ \mathrm{d}S + \int_{\partial\Omega^{(p)}} \left(\underset{\sim}{\sigma}^{0(p)} \cdot \underline{\mathrm{n}}^{(p)} \right) \otimes \underline{\mathrm{y}}^{(p)} \ \mathrm{d}S \\
&+ \int_{\partial\Omega^{(p)}} \left[\left(\underset{\sim}{\sigma}^{1(p)} \ \left(\underline{\mathrm{y}}^{(p)} \cdot \underline{\mathrm{e}}^{(p)} \right) \right) \cdot \underline{\mathrm{n}}^{(p)} \right] \otimes \underline{\mathrm{x}}^{(p)} \ \mathrm{d}S \\
&+ \int_{\partial\Omega^{(p)}} \left[\left(\underset{\sim}{\sigma}^{1(p)} \ \left(\underline{\mathrm{y}}^{(p)} \cdot \underline{\mathrm{e}}^{(p)} \right) \right) \cdot \underline{\mathrm{n}}^{(p)} \right] \otimes \underline{\mathrm{y}}^{(p)} \ \mathrm{d}S
\end{aligned}$$

$$\begin{aligned}
V \underset{\sim}{\Sigma} &= \sum_{p=1}^{4\,N} S^{(p)} \left(\underset{\sim}{\sigma}^{0(p)} \cdot \underline{\mathrm{n}}^{(p)} \right) \otimes \underline{\mathrm{x}}^{(p)} + \left(\underset{\sim}{\sigma}^{0(p)} \cdot \underline{\mathrm{n}}^{(p)} \right) \otimes \int_{\partial\Omega^{(p)}} \underline{\mathrm{y}}^{(p)} \ \mathrm{d}S \\
&+ \left(\underset{\sim}{\sigma}^{1(p)} \cdot \underline{\mathrm{n}}^{(p)} \right) \otimes \underline{\mathrm{x}}^{(p)} \int_{\partial\Omega^{(p)}} \left(\underline{\mathrm{y}}^{(p)} \cdot \underline{\mathrm{e}}^{(p)} \right) \ \mathrm{d}S \\
&+ \left(\underset{\sim}{\sigma}^{1(p)} \cdot \underline{\mathrm{n}}^{(p)} \right) \otimes \int_{\partial\Omega^{(p)}} \left(\underline{\mathrm{y}}^{(p)} \cdot \underline{\mathrm{e}}^{(p)} \right) \ \underline{\mathrm{y}}^{(p)} \ \mathrm{d}S
\end{aligned}$$

with $S^{(p)} = l^{(p)}\, h$ the surface of a fastener.

$$
\begin{aligned}
V\underset{\sim}{\Sigma} &= \sum_{p=1}^{4\,N} S^{(p)} \left(\underset{\sim}{\sigma}^{0(p)} \cdot \underline{\mathrm{n}}^{(p)}\right) \otimes \underline{\mathrm{x}}^{(p)} + \left(\underset{\sim}{\sigma}^{1(p)} \cdot \underline{\mathrm{n}}^{(p)}\right) \otimes \int_{\partial\Omega^{(p)}} \left(\underline{\mathrm{y}}^{(p)} \otimes \underline{\mathrm{y}}^{(p)}\right) \cdot \underline{\mathrm{e}}^{(p)} \, \mathrm{d}S \\
&= \sum_{p=1}^{4\,N} S^{(p)} \left(\underset{\sim}{\sigma}^{0(p)} \cdot \underline{\mathrm{n}}^{(p)}\right) \otimes \underline{\mathrm{x}}^{(p)} + \left(\underset{\sim}{\sigma}^{1(p)} \cdot \underline{\mathrm{n}}^{(p)}\right) \otimes \frac{h \, \left(l^{(p)}\right)^3}{12} \underline{\mathrm{e}}^{(p)} \\
&= \sum_{p=1}^{4\,N} L \, S^{(p)} \left[\left(\underset{\sim}{\sigma}^{0(p)} \cdot \underline{\mathrm{n}}^{(p)}\right) \otimes \frac{\underline{\mathrm{x}}^{(p)}}{L} + \frac{1}{12} \left(l^{(p)} \, \underset{\sim}{\sigma}^{1(p)} \cdot \underline{\mathrm{n}}^{(p)}\right) \frac{l^{(p)}}{L}\right]
\end{aligned}
$$

Appendix B. Determination of $[\mathfrak{k}]$

Having assembled all the elements has lead to four series (sides) of three layers of pantographs. It is then necessary to connect the three layers of the same side. To do so, new mechanical sets are introduced on fig B.25.

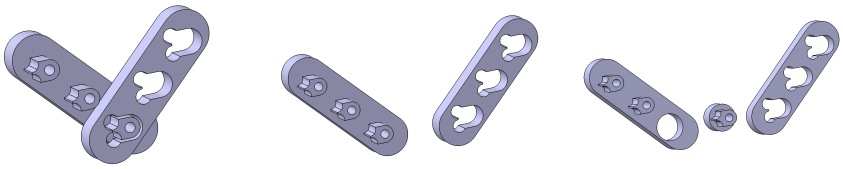

Figure B.25: Three steps of decomposition for the mechanical parts than can be considered

One can not simply impose an identical kinematics on the stacked kinematic nodes, C^k on fig B.26, because the centres of the flexible links of the three layers do not strictly have the same displacement. The points with the same displacement from one layer to another are the statical centres, C^s on fig B.26. However these points do not belong to the lattice, so we can not impose conditions on.

To overcome this problem, a minimal assembly is made (fig B.27) containing:

- the mid-sections of the FL, that are the nodes of the model, in red on fig B.27;
- the anchor parts of the FLs, so the points with strictly the same displacement;

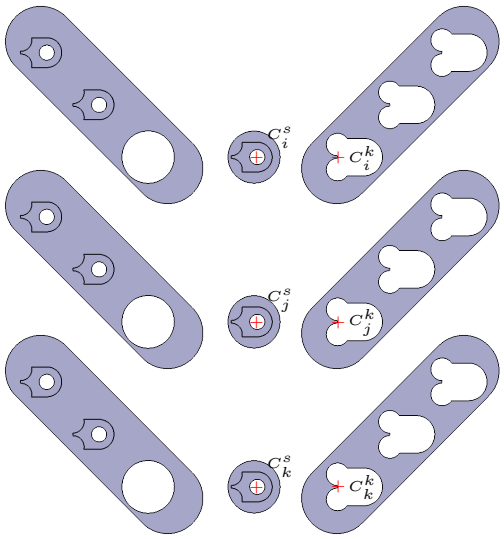

Figure B.26: Stacking of three layers

- a piece of the rigid arms, around the hole of the anchors.

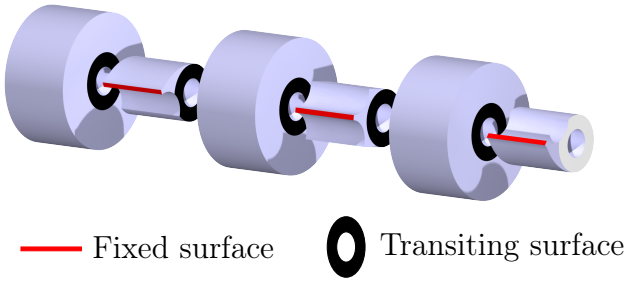

Figure B.27: Assembly used for the determination of the stiffness between the layers

This enables to assess the rigidity between the nodes of the different layers. As for the first step, each simulation result is a row in $[\mathfrak{k}]$.